Lithos 362–363 (2020) 105465

Contents lists available at ScienceDirect

Lithos

journal homepage: www.elsevier.com/locate/lithos

Research Article

Missing Sr—Nd isotopic decoupling in subduction zone: Decoding the multi-stage dehydration and melting of subducted slab in the Chinese Altai

Yang Yu [a], Xiao-Long Huang [a,*], Min Sun [b], Chao Yuan [a]

[a] State Key Laboratory of Isotope Geochemistry, Guangzhou Institute of Geochemistry, Chinese Academy of Sciences, Guangzhou 510640, China
[b] Department of Earth Sciences, The University of Hong Kong, Pokfulam Road, Hong Kong

ARTICLE INFO

Article history:
Received 30 November 2019
Received in revised form 21 February 2020
Accepted 3 March 2020
Available online 4 March 2020

Keywords:
Subduction zone
Fore-arc
Mantle wedge
Sr-Nd isotopic decoupling
Island arc basalt
Central Asian Orogenic Belt

ABSTRACT

Some island arc basalts (IAB) show Nd—Hf isotopic decoupling, which can be attributed to higher mobility of Nd over Hf in melts released from subducted slab and subsequent metasomatism in the mantle wedge. If the same mechanism applies, Sr—Nd isotopic decoupling should be common in typical IAB, but in fact it is not the case. In order to investigate this problem, we carried out a systematic study on the Habahe mafic dykes at ~360 Ma, which emplaced in the south margin of the Chinese Altai due to the northward subduction of the Junggar Ocean. These dykes can be subdivided into four types based on distinct geochemical compositions and spatial distribution. Type-I mafic dykes in the southern area are enriched in light rare earth elements (LREE) and Th with positive Pb anomaly. They have high initial $^{87}Sr/^{86}Sr$ (0.7088–0.7095), $^{206}Pb/^{204}Pb$ (17.971–18.034), $^{207}Pb/^{204}Pb$ (15.526–15.551) and $^{208}Pb/^{204}Pb$ (37.860–37.991) ratios and exhibit Nd—Hf isotopic decoupling with high $\varepsilon_{Hf}(t)$ (+9.5 − +12.1) and low $\varepsilon_{Nd}(t)$ values (+3.5 − +3.9). Thus Type-I mafic dykes are interpreted as originating from a depleted mantle source metasomatized by melts from subducted sediments. Type-II mafic dykes in the western segment of central area are depleted in LREE and Th but enriched in Ba, Sr and Pb. They show high positive $\varepsilon_{Nd}(t)$ (+6.5 − +8.1) and $\varepsilon_{Hf}(t)$ (+13.4 − +15.4) values with relatively low initial $^{87}Sr/^{86}Sr$ (0.7040–0.7049), $^{206}Pb/^{204}Pb$ (17.715–17.839), $^{207}Pb/^{204}Pb$ (15.484–15.495) and $^{208}Pb/^{204}Pb$ (37.739–37.797) ratios, which would be derived from the partial melting of a depleted mantle source with input of fluids from subducted sediments. Type-III mafic dykes in the eastern segment of central area are enriched in LREE with weakly positive Pb anomaly. They show low initial $^{87}Sr/^{86}Sr$ (0.7036–0.7038), $^{206}Pb/^{204}Pb$ (17.871–18.001), $^{207}Pb/^{204}Pb$ (15.485–15.491) and $^{208}Pb/^{204}Pb$ (37.610–37.642) ratios and have high positive $\varepsilon_{Nd}(t)$ (+6.7 − +6.9) and $\varepsilon_{Hf}(t)$ (+14.6 − +14.8) values, which are interpreted as products of partial melting of a depleted mantle source refertilized by melts from the subducted oceanic crust. Type-IV mafic dykes in the northern area are also enriched in LREE but show significantly positive Pb anomaly with intermediate $(^{87}Sr/^{86}Sr)_i$ ratios (0.7068–0.7070), low $\varepsilon_{Nd}(t)$ values (+0.7 − +1.0), high $\varepsilon_{Hf}(t)$ values (+5.5 − +7.8), and high initial $^{206}Pb/^{204}Pb$ (18.001–18.402), $^{207}Pb/^{204}Pb$ (15.522–15.553) and $^{208}Pb/^{204}Pb$ (38.163–38.299) ratios, thus interpreted as originating from a depleted mantle source with the involvement of melts released from subducted sediments. Type-I mafic dykes have similar Nd-Hf-Pb isotopic compositions with Type-IV mafic dykes but show higher $(^{87}Sr/^{86}Sr)_i$ ratios, indicating that the melts and fluids from subducted sediments at shallower depth possess high Sr/Nd ratios because of breakdown of plagioclase. Involvement of such melts and fluids can explain Sr—Nd isotopic decoupling for the southern mafic dykes of this study, as the modern analogue of fore-arc basalts and boninites in the Izu-Bonin-Mariana arc and Western Java, which have higher $^{87}Sr/^{86}Sr$ ratios than those in typical IAB. Consequently, melting of the residual subducted sediments at the sub-arc depth will generate low Sr/Nd fluids and melts, which can account for the Sr—Nd isotopic coupling of the typical IAB and Type-IV mafic dykes of this study.

1. Introduction

The subduction zone is one of the most important site for geochemical fractionation on Earth (Elliott et al., 1997). Island arc basalts (IAB) are characterized by the enrichment of light rare earth elements

* Corresponding author.
E-mail address: xlhuang@gig.ac.cn (X.-L. Huang).

https://doi.org/10.1016/j.lithos.2020.105465
0024-4937/

(LREE) and large ion lithophile elements (LILE) and depletion of high field strength elements (HFSE), which are resulted from complicated interaction between the mantle wedge and subducted slab (altered oceanic crust (AOC) and associated sediments) (e.g., Woodhead et al., 2001). In subduction zone, relatively oxidized and volatile-rich crustal materials are drawn into the deep mantle and undergo dehydration and melting at depth. Fluids and hydrous melts released from the subducted slab will promote melting of the mantle wedge via lowering the solidus of peridotite. Volatiles, LILE and LREE preferably released from the subducted plate into the mantle wedge are carried up by arc magmas to the overlying crust, atmosphere, or oceans, which is important for the geochemical evolution and growth of the continental crust (Grove and Christy, 2012). In contrast, HFSE (Nb, Ta, Zr and Hf) and heavy rare earth elements (HREE) are mostly retained in the residual subducted slab (Hermann and Rubatto, 2009), which ultimately influences the chemical composition of the deep mantle. Such chemical fractionation process also results in decoupling between some pairs of isotopic systems in IAB, such as Nd and Hf isotopes (e.g., Chauvel et al., 2009). Indeed, the Nd—Hf isotopic decoupling of IAB can be explained by different mobilities of Nd and Hf during subduction (Todd et al., 2010). Due to the higher mobility of Nd than Hf during the partial melting of subducted sediments (Skora and Blundy, 2010), the melts from subducted sediments can have high Nd/Hf ratios and modify the Nd isotopic composition more significantly than the Hf isotope in the mantle wedge (Todd et al., 2010), which can result in Nd—Hf isotopic decoupling in IAB (e.g., Chauvel et al., 2009; Todd et al., 2010).

It is a general consensus that the mobility of Sr is much higher than that of Nd in both fluids and melts (e.g., Defant and Drummond, 1990; Hermann et al., 2006; Kessel et al., 2005). Therefore, the subducted slab should release high Sr/Nd fluids or melts into the mantle wedge, which should result in Sr—Nd isotopic decoupling in IAB, as in the case of Nd—Hf isotopic decoupling. However, Sr—Nd isotopic data of IABs suggest that they commonly plot along or even below the mixing line between the depleted mantle source and the subducted sediments (Nielsen and Marschall, 2017), indicating that Sr—Nd isotopic decoupling is missing in subduction zone. In order to circumvent the problem related to high Sr/Nd ratio in fluids/melts, Nielsen and Marschall (2017) recently proposed that the melts and fluids from subducted slab cannot account for the formation of arc lavas and that the subducted sediments may rise as diapirs (high-pressure mélange) into the mantle wedge and then melt to form arc magmas. This model excludes the dehydration and melting of subducted slab, which can avoid the fractionation between Sr and Nd during subduction, but strongly contradicts the consensus that IAB are mainly formed through fluxing melting of the mantle wedge with the input of fluids and hydrous melts from subducted slab. Therefore, it is worth of further investigation on why Nd—Hf isotopic decoupling is common but Sr—Nd isotopic decoupling is insignificant for IAB.

It is suggested that the involvement of subducted components in the mantle wedge varies from the fore-arc to back-arc, as shown by the cross-arc geochemical variations of arc rocks (Labanieh et al., 2012; Sendjaja et al., 2009). The compiled data show that the fore-arc basalts and high-Ca boninites from the Izu-Bonin-Mariana arc and the Western Java have an overall higher $^{87}Sr/^{86}Sr$ ratios than those of typical IAB (Fig. 1). This suggests that the input components at shallow depth in the fore-arc possibly have higher Sr/Nd ratios than those at deeper depth in the sub-arc, corresponding to distinct fractionation between Sr and Nd at different depths in subduction zone. In this study, we carried out systematic geochemical and isotopic analyses for a group of mafic dykes from the Chinese Altai to decipher the mechanism of fractionation between Sr and Nd during the slab subduction.

The Chinese Altai is located in the southwestern part of the Central Asian Orogenic Belt (CAOB; Fig. 2a; Jahn et al., 2000) and underwent large-scale arc magmatism in the middle Paleozoic (Fig. 2b) as a result of the northward subduction of the Junngar Ocean, a segment of the Paleo-Asian Ocean (Kröner et al., 2017; Xiao et al., 2004, 2015). The middle Paleozoic subduction induced significant mafic magmatism in the Chinese Altai (Cai et al., 2010). These mafic rocks have wide range of geochemical compositions due to extensive metasomatism in their mantle sources with input of different subducted components, including fluids and melts from subducted sediments or subducted oceanic crust (Yu et al., 2017). A group of mafic dykes intruded into the Devonian Habahe igneous complex in southern margin of the Chinese Altai (Fig. 2c; Cai et al., 2010; Yu et al., 2017). The mafic dykes in the south have high $\varepsilon_{Nd}(t)$ values (from +7.7 to +8.1) and are characterized by LILE enrichment and LREE depletion with high Ba/La ratios, which were derived from the partial melting of the depleted mantle refertilized by fluids from subducted sediments. In contrast, the mafic dykes in the north are characterized by LREE enrichment and Nd—Hf isotopic decoupling with high $\varepsilon_{Hf}(t)$ (from +5.5 to +7.8) and low $\varepsilon_{Nd}(t)$ (from +0.7 to +1.0) values, which were likely originated from a depleted mantle source metasomatized by melts from subducted sediments (Yu et al., 2017). Therefore, the Habahe mafic dykes might record the processes of diverse geochemical fractionation during the multi-stage dehydration and melting of subducted slab in a small area. In this study, we report bulk-rock major and trace elements and Sr-Nd-Hf-Pb isotopes for the Habahe mafic dykes systematically sampled from south to north (Fig. 2c). By integrating these analyses with previously published data (Cai et al., 2010; Yu et al., 2017), we describe the elemental fractionation and consequent isotopic decoupling in

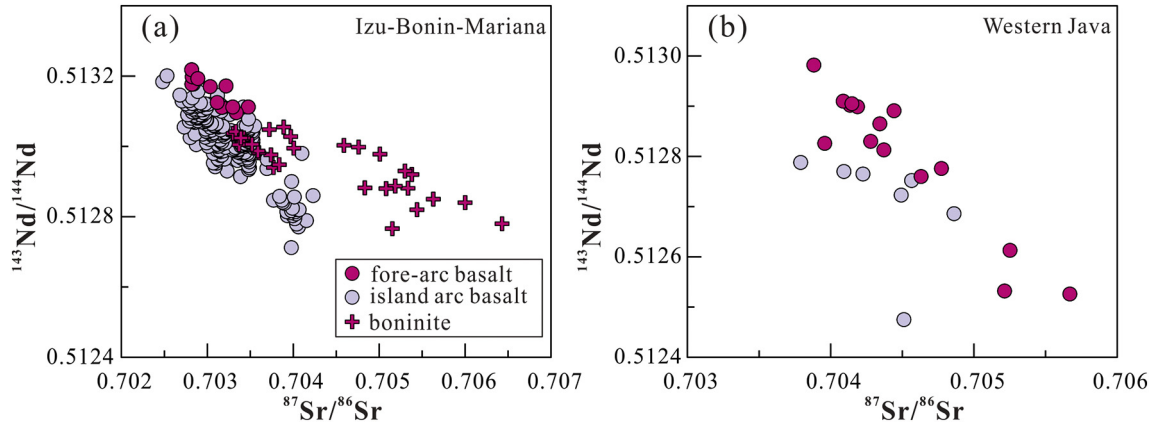

Fig. 1. Diagrams of $^{87}Sr/^{86}Sr$ vs. $^{143}Nd/^{144}Nd$ for the Cenozoic island arc basalts (IAB) and fore-arc basalts (FAB) from the Mariana and Western Java arcs and boninites from the Izu-Bonin-Mariana (IBM) arcs. (a) the IBM arcs, IAB (SiO_2 = 45–53 wt%) and boninite are from the PetDB database (http://www.petdb.org), and FAB from Reagan et al. (2010); (b) the Western Java, FAB and IAB are all from Sendjaja et al. (2009).

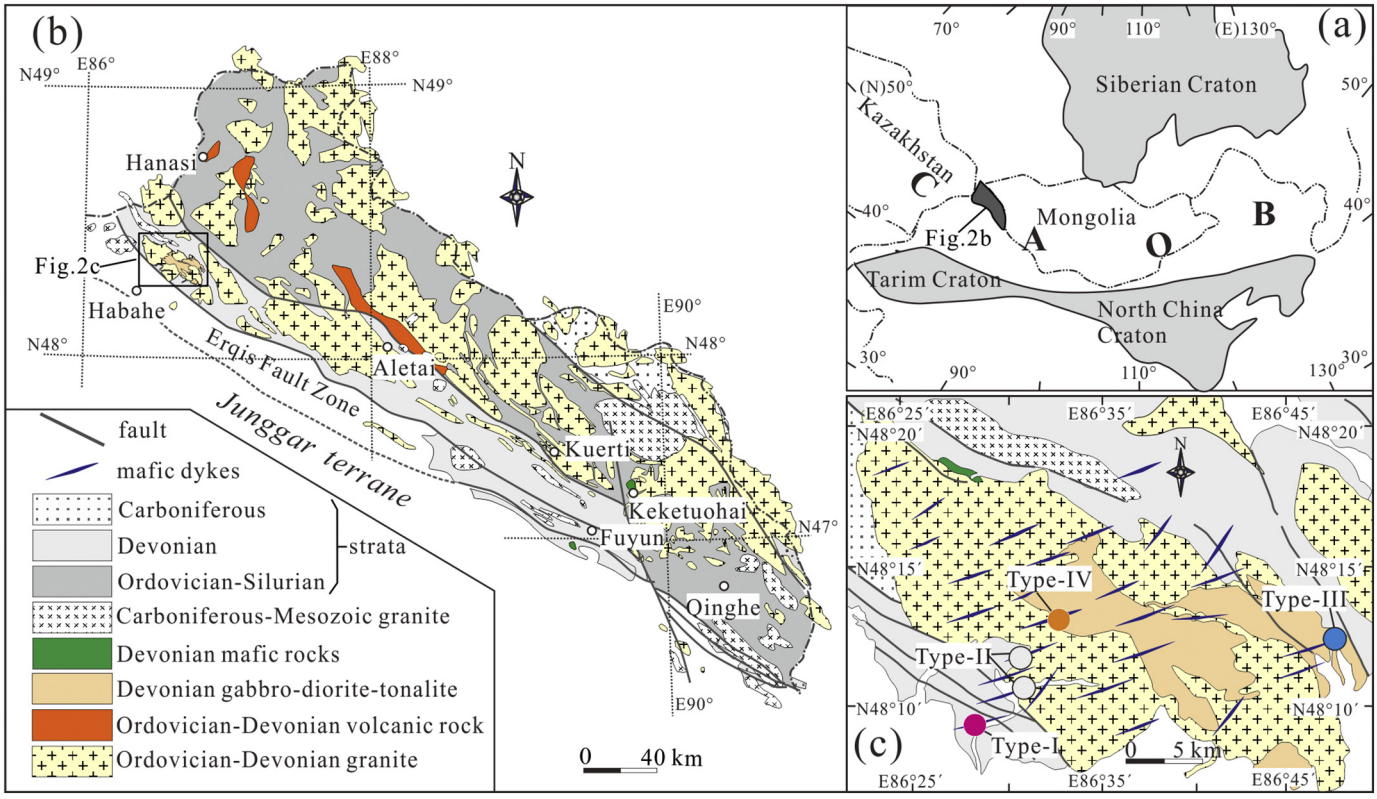

Fig. 2. (a) Simplified regional map showing the known extent of the CAOB. (b) Geological map characterizing the tectonic framework of the Chinese Altai (revised from Huang et al., 2020; Li et al., 2019; Sun et al., 2008; Zhang et al., 2017). (c) Simplified geological maps of the Habahe complex showing rock types and sample locations for four types of mafic dykes in the Habahe complex (Yu et al., 2017). Location and strike of the Habahe mafic dykes are based on Cai et al. (2010) and field observation.

subduction zone associated with multi-stage dehydration and melting of subducted slab, which are crucial for understanding the mass transfer from the subducted slab to the mantle wedge.

2. Geological setting and sample description

The Chinese Altai is located in the southwestern CAOB (Fig. 2a) and is bounded by the Erqis Fault in the south, separating from the Junggar terrane (Fig. 2b). The region is commonly envisaged as an early Paleozoic active continental margin or accretionary complex and underwent prolonged subduction from ~470 Ma to ~330 Ma (Xiao et al., 2004). The Chinese Altai was subdivided into six tectonic units based on lithology and Nd isotope of granite, which had been described in previous literatures in details (e.g. Wang et al., 2009; Windley et al., 2002). The Devonian arc magmatism is significant in the Chinese Altai, including voluminous granites covering approximately 40% outcropping area of the region, and some mafic rocks that mainly outcropped in the southern Chinese Altai (Fig. 2b). The arc magmatism has significantly enhanced the proportion of juvenile materials in the crust of the Chinese Altai, as evidenced by a sharp increase of zircon $\varepsilon_{Hf}(t)$ values in the Paleozoic sedimentary rocks (Sun et al., 2008, 2009).

The Habahe igneous complex in the northeastern Habahe town is composed of fine-grained biotite granite (381 ± 4 Ma to 359 ± 4 Ma), gabbroic rocks (369 ± 3 Ma), diorite and tonalite (371 ± 3 Ma), which emplaced into the Devonian sequence and were exposed in an area of ~450 km^2 (Fig. 2c, Yu et al., 2017, 2019). The Habahe mafic dykes outcropped in an area extending ~30 km from the south to the north (Fig. 2c) and vertically intruded into the Habahe complex and the surrounding country rocks (Fig. 3). They generally show NE-NEE striking (Cai et al., 2010) and have widths ranging from 0.5 m to 5 m (Fig. 3). Cai et al. (2010) conducted U—Pb age analyses on the Habahe mafic dykes and obtained an age of 375.5 ± 4.8 Ma. However, these dykes possibly intruded later since they cut through the tonalite (371 ± 3 Ma; Yu et al., 2019) and the gabbroic rocks (369 ± 3 Ma; Yu et al., 2017). Samples collected in this study are mostly massive and aphanitic (Supplementary Fig. S1).

3. Analytical methods

All the analyses were performed at the State Key Laboratory of Isotope Geochemistry (SKLaBIG), Guangzhou Institute of Geochemistry, Chinese Academy of Sciences (GIG-CAS). Analytical procedure and conditions of zircon U—Pb dating, major and trace elemental and Sr-Nd-Hf-Pb isotopic analyses are principally similar to those described by Yu et al. (2017).

3.1. Zircon U—Pb dating

Zircon U—Pb analyses of the Habahe mafic dykes and granodiorite were carried out using the Cameca IMS 1280HR ion microprobes. A secondary standard zircon Qinghu (Li et al., 2013) were analyzed once every five or six spots as unknown to monitor the reliability of the whole procedure, yielding a weighted mean age of 159.2 ± 1.8 Ma (n = 8), identical to the recommended value of 159.5 ± 0.2 Ma (Li et al., 2013). Data reduction was carried out using Isoplot/Ex 3.6 software (Ludwig, 2008).

3.2. Whole-rock major and trace elements

Whole-rock major element concentrations were analyzed using a Rigaku RIX 2000 X-ray fluorescence spectrometer (XRF) with analytical uncertainties between 1% and 5%. Trace element analyses were conducted by Perkin-Elmer Sciex ELAN 6000 ICP-MS after acid digestion of samples in high-pressure Teflon vessels. The USGS and Chinese

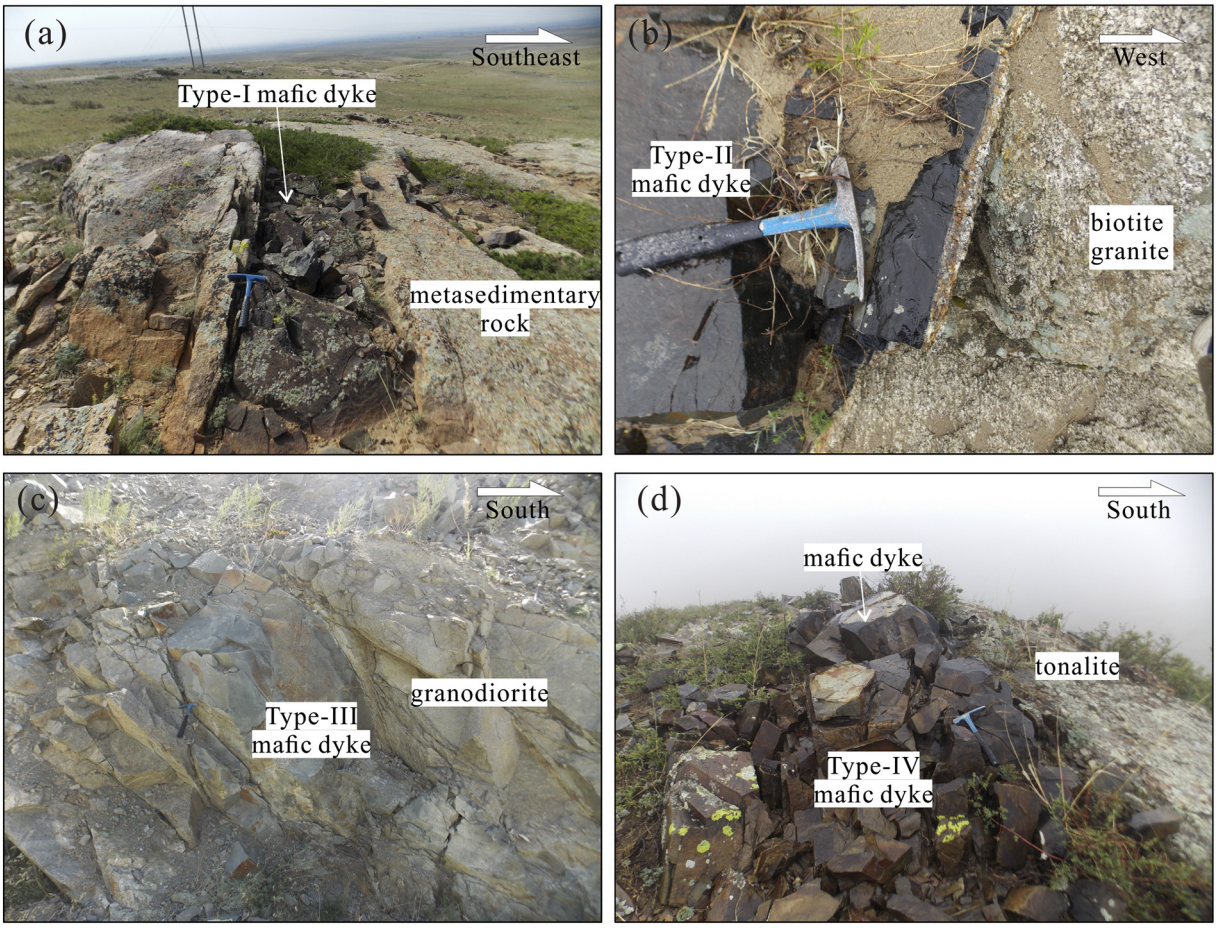

Fig. 3. Field photographs showing (a) Type-I mafic dykes intruding into the upper crustal metasedimentary rock; (b) Type-II mafic dyke cutting biotite granite; (c) Type-III mafic dyke intruding into granodiorite, and (d) Type-IV mafic dykes cutting tonalite.

National standards AGV-2, GSR-1, GSR-2, GSR-3, BHVO-2, W-2a and SARM-4 were chosen for calibrating element concentrations of the analyzed samples. Analytical precision of the REE and other incompatible element analyses is typically 1%–5%.

3.3. Whole-rock Sr-Nd-Hf-Pb isotopes

Whole-rock Sr, Nd, Hf and Pb isotopic analyses were determined on a subset of whole-rock sample powder by a Neptune plus MC-ICP-MS. All chemical preparations were performed on the specially designed class-100 work benches inside a class-1000 clean laboratory.

For Sr, Nd, Hf and Pb isotopes, powder of a sample was weighted (about 80 mg, 200 mg for Hf less than 1 ppm into two capsules) into a 7 ml round bottom SavillexTM Teflon screw-top capsule. One drop purified water was added to make sample wet. Then, mixed concentrate HF-HNO_3 (1–2 ml) was added and the capsule screw-top cap was closed. The capsule was placed into a steel-jacketed bomb for 48 h in a furnace under 190 °C. For Pb isotope, the total procedural blank was less than 0.4 ng. Samples were doped with Tl, and mass discrimination was corrected using a certified $^{203}Tl/^{205}Tl$ ratio of 0.418922. During the period of analysis, repeated analyses of National Institute of Standards and Technology Standard Reference Material 981 yielded $^{206}Pb/^{204}Pb = 16.9325 \pm 5$ (2σ), $^{207}Pb/^{204}Pb = 15.4859 \pm 6$ (2σ), and $^{208}Pb/^{204}Pb = 36.6825 \pm 18$ (2σ). Measured $^{87}Sr/^{86}Sr$, $^{143}Nd/^{144}Nd$ and $^{177}Hf/^{176}Hf$ ratios were normalized to $^{86}Sr/^{88}Sr = 0.1194$, $^{146}Nd/^{144}Nd = 0.7219$ and $^{179}Hf/^{177}Hf = 0.7325$, respectively, using the exponential law. The analyzed reference standards (BHVO-2) and duplicated analyses are compiled in Supplemental Table 1.

4. Analytical results

The zircon U—Pb age, whole-rock major and trace element and the Sr-Nd-Hf-Pb isotope data of the Habahe mafic dykes are presented in the Supplemental Tables 2–4.

4.1. Zircon U—Pb age

Although large samples (>5 kg) of the Habahe mafic dykes were selected for zircon separation, only 20–30 grains were picked up from samples HB15–10 and HB15–32, respectively. To constrain emplace age of other dykes, zircons of granodiorite (sample HB15–227) that was cut by mafic dykes (Fig. 3c) were also analyzed. The analytical results of two mafic dyke samples and one granodiorite sample are presented in Supplemental Table 2.

Seventeen zircons from sample HB15–10 were analyzed and show variable Th (22–1741 ppm) and U contents (89–3759 ppm) and Th/U ratios (0.11–0.81). Eight grains show nebulous zoning and have high U contents (264–3759 ppm) with variable Th/U ratios (0.11–0.81), which gave relatively old $^{206}Pb/^{238}U$ ages from 417 ± 6 Ma to 468 ± 7 Ma (Fig. 4a). Because the mafic dyke intruded into the Devonian strata (Fig. 2c, 3a), these grains are interpreted as inherited zircons, and were possibly captured from the crust during the emplacement of mafic magma. The other nine zircons are stubby and have strong oscillatory zoning on CL images (Fig. 4a). These zircons have low U (89–996 ppm) with overall high Th/U ratios (0.24–0.57) and show relatively coherent young $^{206}Pb/^{238}U$ ages (from 357 ± 8 Ma to 366 ± 7 Ma), yielding a weighted mean $^{206}Pb/^{238}U$ age of 361 ± 4 Ma (MSWD = 0.20; Fig. 4a), which is interpreted as the crystallization age.

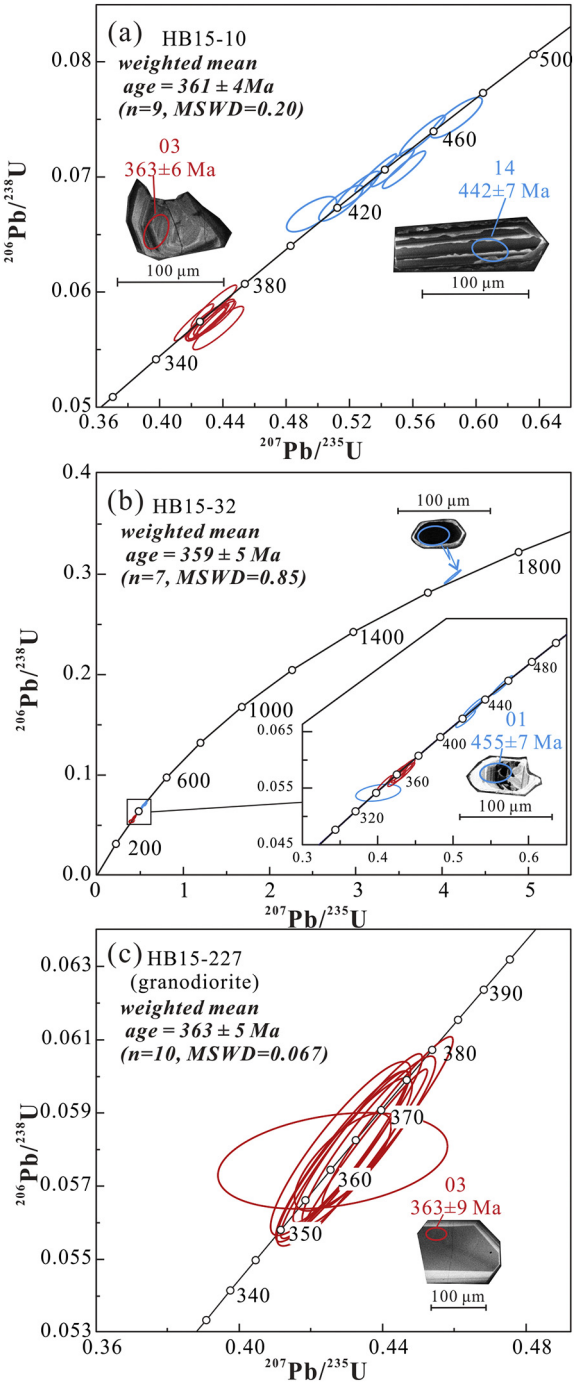

Fig. 4. Concordia diagrams showing the weighted mean ages of zircons from (a) HB15–10 (mafic dyke), (b) HB15–32 (mafic dyke), and (c) HB15–227 (granodiorite) with uncertainties at the 1σ.

Twelve zircons from sample HB15–32 show variable Th/U ratios (0.21–1.48) and have Th and U contents ranging from 35 to 1456 ppm and from 164 to 1381 ppm, respectively. Spot 09 on inherited core of a rounded zircon exhibits old $^{207}Pb/^{206}Pb$ age of 1633 ± 5 Ma. Spots 01, 04, 06 and 10 on inherited cores with slightly rounded termination show relatively old $^{206}Pb/^{238}U$ ages from 420 ± 6 Ma to 455 ± 7 Ma (Fig. 4b), which are all interpreted as inherited zircons because the mafic dykes cut through the biotite granite of 381 ± 4 Ma (Yu et al., 2019; Fig. 3b). Spot 03 gave a relatively young $^{206}Pb/^{238}U$ age of 340 ± 6 Ma, which is possibly due to the disturbance of the U—Pb isotopic system during a later thermal event. The other six analyses formed a cluster and yielded a weighted mean $^{206}Pb/^{238}U$ age of 359 ± 5 Ma (MSWD = 0.85; Fig. 4b), which is interpreted as the crystallization age of the sample.

Zircons from granodiorite sample HB15–227 show oscillatory zoning (Fig. 4c) and have variable Th (55.1–369 ppm) and U contents (92.8–382 ppm) with high Th/U ratios from 0.59 to 0.97 (Supplemental Table 2). All U—Pb dating results are concentrated on concordia and yielded a weighted mean $^{206}Pb/^{238}U$ age of 363 ± 5 Ma (MSWD = 0.067; Fig. 4c), which is interpreted as the crystallization age.

4.2. Whole-rock compositions

Whole-rock major and trace elements and Sr-Nd-Hf-Pb isotopes of the Habahe mafic dykes are presented in Supplemental Tables 3 and 4. The Habahe mafic dykes can be broadly subdivided into four types, from the south to the north, according to their distinctive geochemical and isotopic characteristics.

4.2.1. Type-I mafic dykes

Type-I mafic dykes, collected from the southern area (Fig. 2c), have intermediate MgO (4.56–5.81 wt%) and low Al_2O_3 (15.4–16.5 wt%), CaO (5.09–8.42 wt%) and K_2O (0.06–0.21 wt%) contents, with low K_2O/Na_2O and high FeO^T/MgO ratios, belonging to the low-K tholeiitic series (Fig. 5). They show enrichment of LREE, Rb, Th and U and are depleted in Nb, with weakly positive Eu anomalies (δEu = 1.01–1.11) on chondrite-normalized REE and significantly positive Pb and Sr anomalies on primitive mantle-normalized multi-elements variation diagram (Fig. 6a, b).

Type-I mafic dykes are characterized by the highest initial $^{87}Sr/^{86}Sr$ ratios (0.7088–0.7095) of the studied samples and have positive $\varepsilon_{Nd}(t)$ (+3.5 — +3.9) and $\varepsilon_{Hf}(t)$ values (+9.5 — +12.1), with moderate initial $^{206}Pb/^{204}Pb$ (17.971–18.034), $^{207}Pb/^{204}Pb$ (15.526–15.551) and $^{208}Pb/^{204}Pb$ (37.860–37.991) ratios (Fig. 7).

4.2.2. Type-II mafic dykes

Type-II mafic dykes, sampled from the western segment of central area (Fig. 2c), have high MgO contents (6.44–9.10 wt%) and high $Mg^{\#}$ values (0.57–0.63). These samples have tholeiitic compositions (Fig. 5e) and exhibit low K_2O contents with low K_2O/Na_2O ratios. They show enrichment of LILE (e.g., Sr, Ba, U and Pb) and depletion of LREE and Th (Fig. 6c, d).

Type-II dyke samples show low initial $^{87}Sr/^{86}Sr$ (0.7041–0.7048), $^{206}Pb/^{204}Pb$ (17.715–17.839), $^{207}Pb/^{204}Pb$ (15.484–15.495) and $^{208}Pb/^{204}Pb$ (37.739–37.797) ratios, but have highly positive $\varepsilon_{Nd}(t)$ (from +6.5 to +8.1) and $\varepsilon_{Hf}(t)$ (from +13.4 to +15.4) values (Fig. 7).

4.2.3. Type-III mafic dykes

Type-III mafic dykes, sampled from the eastern segment of central area (Fig. 2c), are basaltic to andesitic in composition and have high MgO contents (5.25–6.49 wt%) and high $Mg^{\#}$ values (0.63–0.66; Fig. 5). These samples have low K_2O contents with low FeO^T/MgO and K_2O/Na_2O ratios, which belong to a low-K Calc-alkaline series (Fig. 5). They show weakly negative Eu anomaly (0.90–1.00) and enrichment of LREE with high $[La/Yb]_N$ values (2.46–4.59) (Fig. 6c). These dykes are also characterized by enrichment of Ba, Rb, Pb, Th and U and depletion of Nb and Ti on primitive mantle-normalized multi-elements variation diagram (Fig. 6d).

Type-III mafic dykes have low initial $^{87}Sr/^{86}Sr$ (0.7036–0.7038), $^{206}Pb/^{204}Pb$ (17.871–18.001), $^{207}Pb/^{204}Pb$ (15.485–15.491) and $^{208}Pb/^{204}Pb$ ratios (37.610–37.642) with highly positive $\varepsilon_{Nd}(t)$ (from +6.7 to +6.9) and $\varepsilon_{Hf}(t)$ (from +14.6 to +14.8) values (Fig. 7).

4.2.4. Type-IV mafic dykes

Type-IV mafic dykes in the northern area (Fig. 2c) have been previously reported by Cai et al. (2010) and Yu et al. (2017), which show intermediate contents of MgO (4.66–5.02 wt%). These dykes are enriched

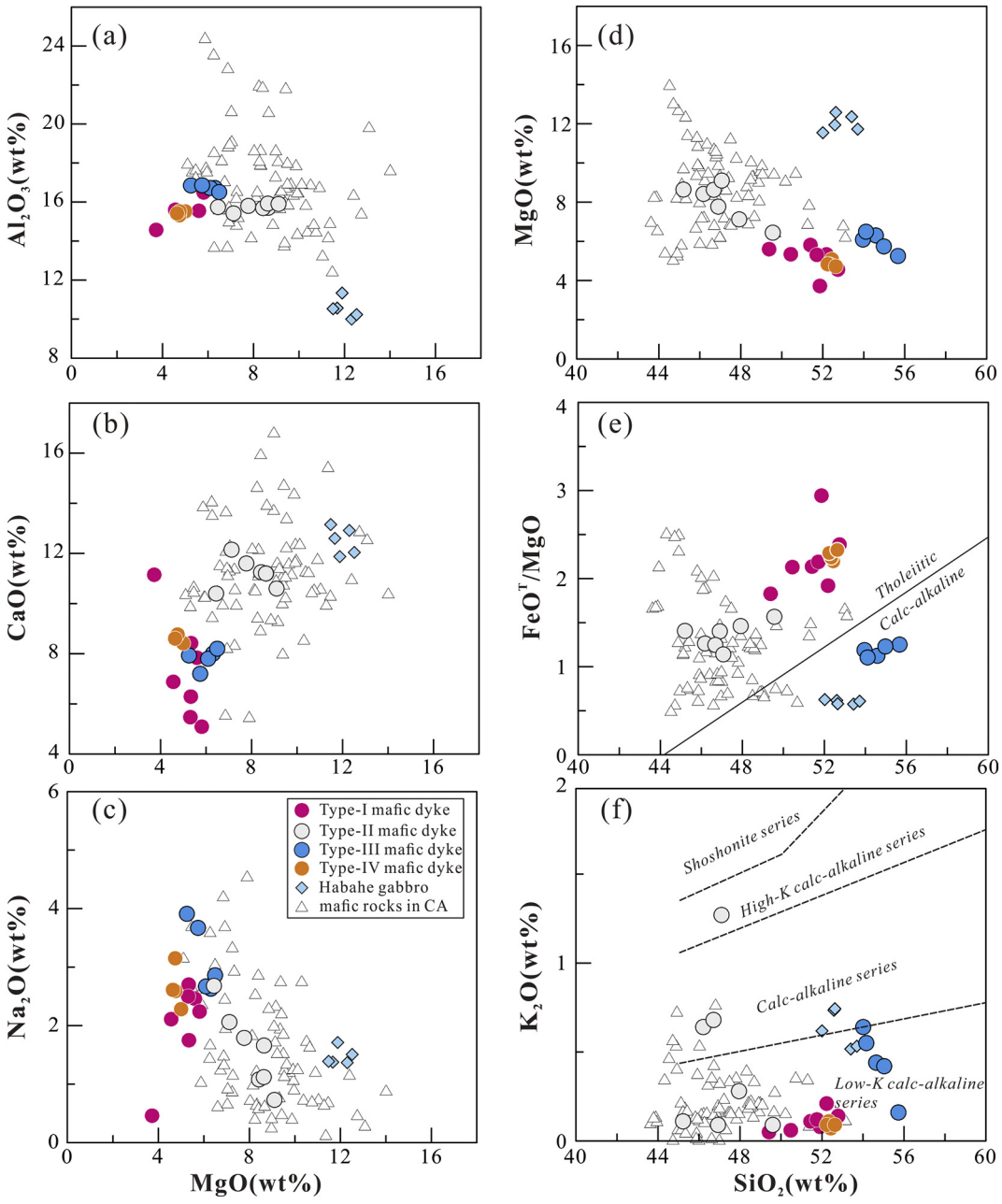

Fig. 5. Harker diagrams of (a) Al_2O_3 vs. MgO, (b) CaO vs. MgO, (c) Na_2O vs. MgO, (d) MgO vs. SiO_2, (e) FeO^T/MgO vs. SiO_2, and (f) K_2O vs. SiO_2 for the Habahe mafic dykes. Published data for the Devonian mafic rocks in the Chinese Altai (CA) are compiled in Supplemental Table 6.

in Th and LREE, but depleted in Nb and Ti and show positive Sr and Pb anomalies (Fig. 6a, b).

Type-IV mafic dykes have variable $(^{87}Sr/^{86}Sr)_i$ (0.7068–0.7070) ratios, positive $\varepsilon_{Nd}(t)$ (from +0.7 to +1.0) and $\varepsilon_{Hf}(t)$ values (from +5.5 to +7.8) and are characterized by high initial $^{206}Pb/^{204}Pb$ (18.001–18.402), $^{207}Pb/^{204}Pb$ (15.522–15.553) and $^{208}Pb/^{204}Pb$ (38.163–38.299) ratios (Fig. 7; Yu et al., 2017).

5. Discussion

5.1. Emplacement of the Habahe mafic dyke

Type-I and -II mafic dykes (361 ± 4 Ma and 359 ± 5 Ma, respectively) show slightly younger age than the Habahe gabbro (369 ± 3 Ma; Yu et al., 2017), indicating their later emplacement. Type-IV mafic dykes intruded into the Habahe gabbro and tonalite (371 ± 3 Ma; Yu et al., 2019), denoting that these dykes emplaced after 370 Ma. In addition, Type-III mafic dykes cut through granodiorite with age of 363 ± 5 Ma (Fig. 4c), indicating their formation later than the Habahe gabbro. Therefore, the field relationships and geochronology data suggest that the mafic rocks in the Habahe complex emplaced in two stages, i.e. ~370 Ma (gabbroic rocks) and ~360 Ma (mafic dykes). Given the similar NE-NEE striking direction for the sampled mafic dykes, we suggest that these dykes were formed during the same subduction event at ~360 Ma.

It is hard to constrain the emplacement temperature and pressure of the Habahe mafic dykes because of their lack of phenocrysts (Fig. S1). However, the field relationship of these dykes suggests their emplacement at the upper crustal level. Type-I mafic dykes intruded into the Devonian sedimentary strata (Fig. 3a) which underwent low grade

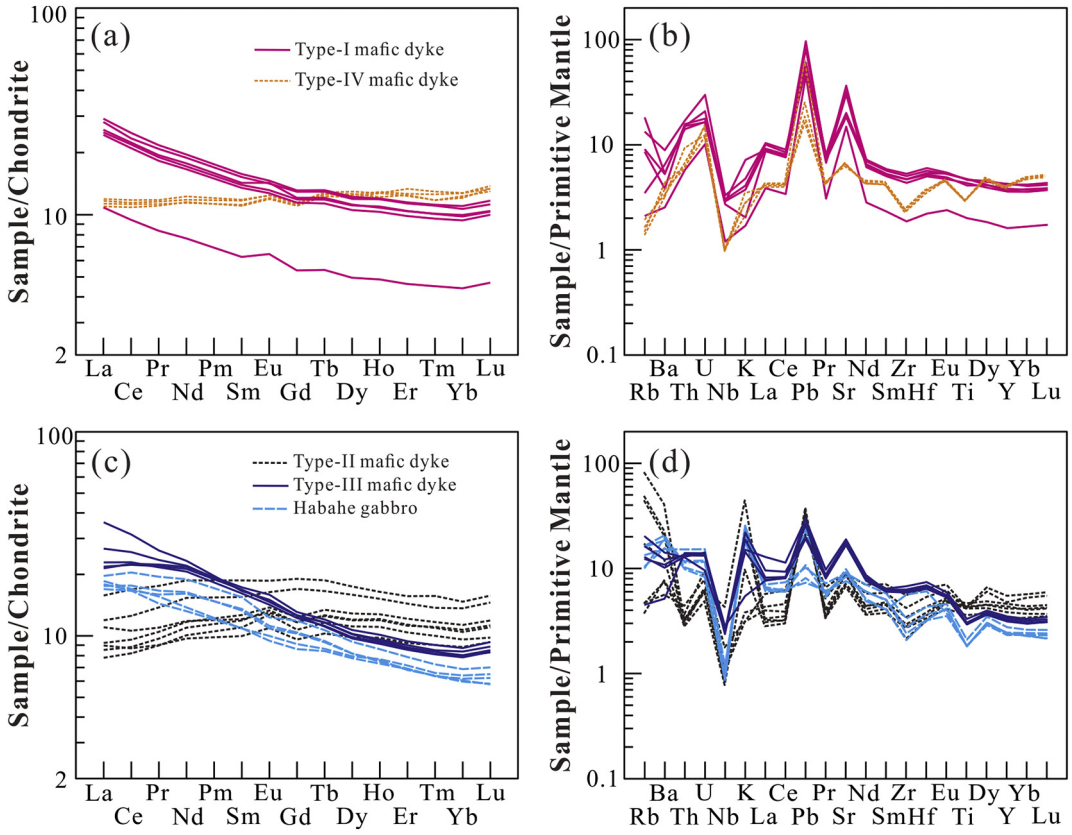

Fig. 6. Chondrite-normalized REE patterns and primitive mantle-normalized trace elements variation diagrams for the Habahe mafic dykes. Chondrite and PM values are from Sun and McDonough (1989) and McDonough and Sun (1995), respectively.

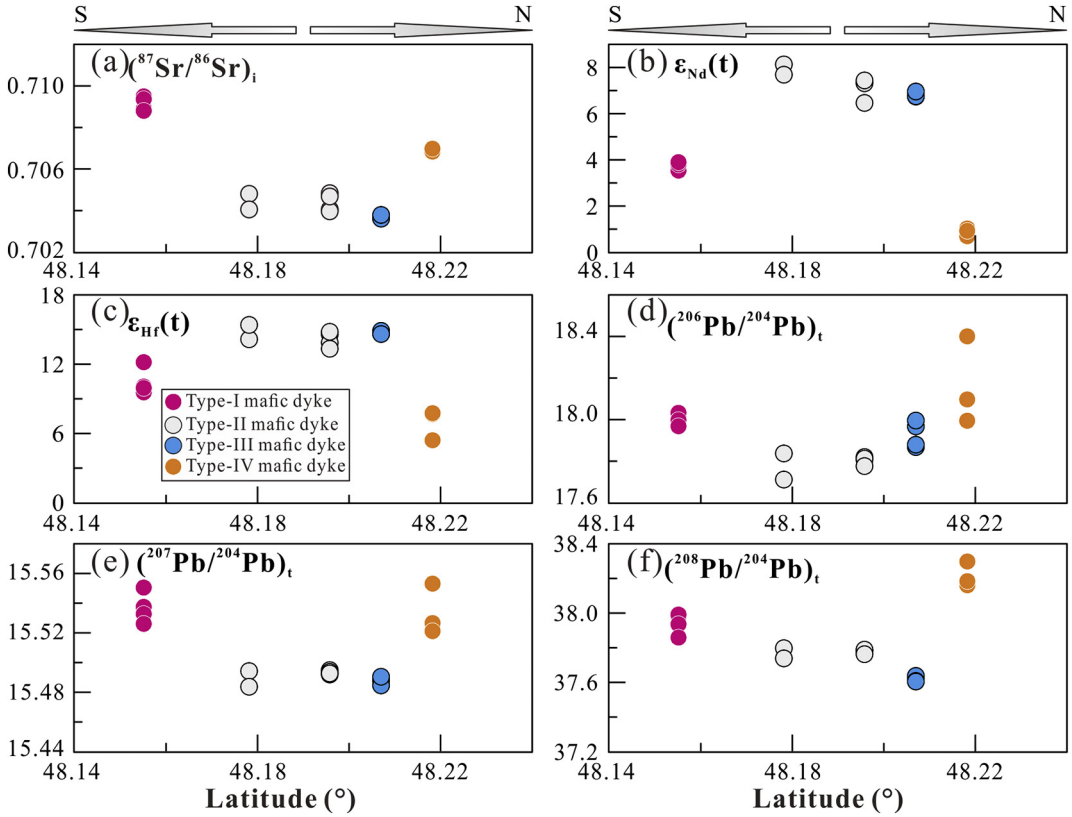

Fig. 7. Spatial variations (Latitude) of (a) $(^{87}Sr/^{86}Sr)_i$, (b) $\varepsilon_{Nd}(t)$, (c) $\varepsilon_{Hf}(t)$, (d) $(^{206}Pb/^{204}Pb)_t$, (e) $(^{207}Pb/^{204}Pb)_t$, and (f) $(^{208}Pb/^{204}Pb)_t$ for the Habahe mafic dykes.

greenschist metamorphism, consistent with the emplacement of the upper crustal level. Type-II mafic dykes cut the Devonian biotite granite (Fig. 3b) that was intruded by tonalite (371 ± 3 Ma; Yu et al., 2019). The tonalite (371 ± 3 Ma) emplacing into the upper crustal level (1.5–2.1 kbar; Yu et al., 2019) was cut by Type-IV mafic dykes (Fig. 3d), indicating that both Type-II and -IV mafic dykes also intruded into the upper crust. Type-III mafic dykes cut granodiorite (Fig. 3c) that consists of amphibole, biotite, plagioclase and quartz. Low Al_2O_3 content of amphiboles (5.80–7.00 wt%; unpublished data) suggests that the granodiorite and Type-III mafic dykes also intruded into the upper crust level (<3 kbar).

Type-I and -II mafic dykes contain some inherited zircons, indicating input of some crustal materials during the magma evolution. Since crustal materials are commonly characterized by high K_2O, significant crustal assimilation can be excluded due to the low K_2O contents in the Habahe mafic dykes (Fig. 5f). In addition, these samples all have positive $\varepsilon_{Hf}(t)$ values (Fig. 7c) and show poor correlations between K_2O contents and Sr, Nd, Pb and Hf isotopes (Fig. 8), consistent with negligible assimilation of isotopically distinct crustal materials during magmatic evolution. Therefore, the Habahe mafic dykes should mostly preserve the Sr, Nd, Hf and Pb isotopic compositions of their mantle source.

5.2. Multiple dehydration and melting of subducted slab

5.2.1. Mantle source characteristics

Most petrogenetic models for typical IAB require mainly two source components: the mantle wedge and the subducted slab (including AOC and overlying sediments). The subducted slab commonly undergo multiple stage dehydration and melting during its descent, which continuously releases fluids and melts to metasomatize the overlying mantle wedge. In the middle Paleozoic, the northward subduction of the Junggar oceanic plate triggered significant arc magmatism in the Chinese Altai (Sun et al., 2008; Wang et al., 2009; Xiao et al., 2004). The spatial variations of Sr, Nd, Hf and Pb isotopic compositions for the Habahe mafic dykes suggest that their mantle source had been metasomatized by different components from the subducted slab (AOC and sediments). Chemical composition of the oceanic crust can be modified by various alteration processes, from its formation near the spreading center to its consumption at the subduction zone (Hauff et al., 2003; Kelley et al., 2003). Comparison of the altered basalts near the subduction zone with the unaltered mid-ocean ridge basalt (MORB) suggests that Sr and Pb isotopes of the AOC can be easily changed by seawater alteration and hydrothermal alteration due to high mobility of Rb, Sr, U and Pb in fluids (e.g., Hauff et al., 2003; Hoernle, 1998). On the other hand, hydrothermal alteration show insignificant influence on Nd—Hf isotopic systems because Sm, Nd, Lu and Hf are relatively immobile during the seafloor alteration (Chauvel et al., 2009; Hauff et al., 2003; Kelly et al., 2003). Thus, the initial Nd and Hf isotopic data for the AOC will mostly reflect the Nd and Hf isotopic compositions of its source (Hauff et al., 2003). The modern subducting sediments (GLOSS), dominantly consisting of terrigenous materials (76 wt% terrigenous, 7 wt% calcium carbonate, 10 wt% opal and 7 wt% mineral-bound H_2O; Plank and Langmuir, 1998), are suggested to have geochemical and isotopic compositions similar to the upper continental crust, e.g. with low $\varepsilon_{Nd}(t)$ and $\varepsilon_{Hf}(t)$ values (Chauvel et al., 2009; Hauff et al., 2003; Plank and Langmuir, 1998).

The Habahe mafic dykes are enriched in LILE and depleted in HFSE, suggesting significant input of LILE from the subducted slab to the overlying mantle wedge, but HFSE and HREE might be preserved in garnet, rutile and zircon residues of the subducted slab (Foley et al., 2000; Hermann and Rubatto, 2009; Johnson, 1998). Thus, the components from subducted slab cannot significantly change the mantle wedge in HREE and HFSE compositions, which can be used to determine the pre-subduction composition of mantle wedge. Although the inherited zircons may decrease $^{176}Hf/^{177}Hf$ ratios, the studied mafic dykes all have positive $\varepsilon_{Hf}(t)$ values (Fig. 7c), indicating their origination from a depleted mantle source. The Habahe mafic dykes all show flat heavy

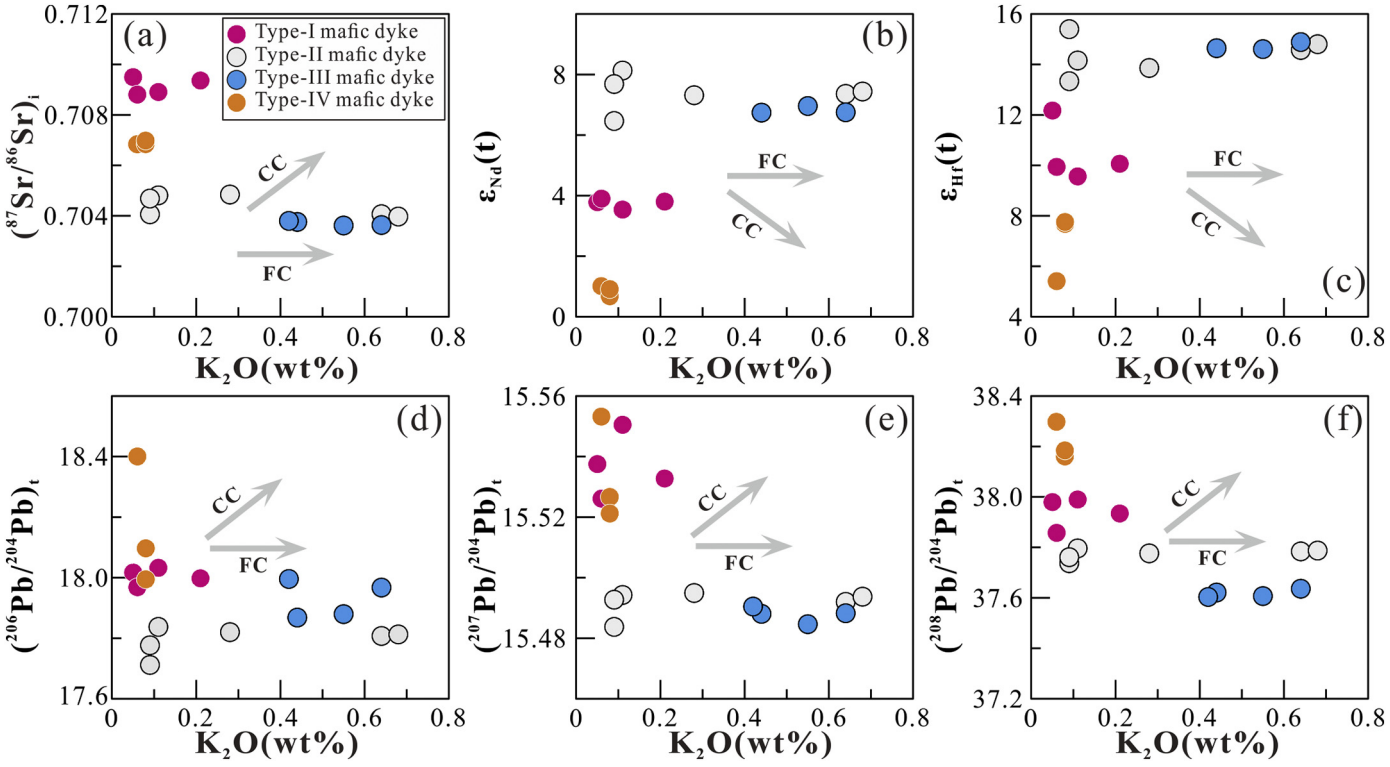

Fig. 8. Diagrams of $(^{87}Sr/^{86}Sr)_i$, $\varepsilon_{Nd}(t)$, $\varepsilon_{Hf}(t)$, $(^{206}Pb/^{204}Pb)_t$, $(^{207}Pb/^{204}Pb)_t$ and $(^{208}Pb/^{204}Pb)_t$ versus K_2O for the Habahe mafic dykes, showing insignificant effect of crustal contamination on the isotopic compositions of the Habahe mafic dykes. CC = crustal contamination; FC = fractional crystallization.

REE (HREE) patterns and low Er/Yb ratios (<1.1; Fig. 6), which precludes the involvement of garnet during the melting of their mantle source and the evolution of their parent magmas. In mafic melt system, Zr, Nb and Y all behave as highly incompatible elements, and thus, the fractional crystallization of pyroxene and olivine has negligible influences on Zr/Y and Nb/Y ratios for mafic magma (Dunn and Sen, 1994; Green et al., 2000). Indeed, the Habahe mafic dykes have uniform Zr/Y and Nb/Y ratios similar to MORB (Supplementary Fig. S2). Therefore, the pre-subduction mantle wedge in the Chinese Altai possibly had geochemical and Sr, Nd, Hf and Pb isotopic compositions similar to the depleted mantle (DM).

5.2.2. Identification of the components derived from subducted slab

5.2.2.1. Fluids and melts from subducted sediments. The Habahe mafic dykes show large and systematic variations in Sr, Nd and Pb isotopic compositions, which indicates the involvement of different components from the subducted slab in their mantle source. Type-I and -IV mafic dykes are characterized by significantly positive Pb anomaly (Fig. 6), relatively low $\varepsilon_{Nd}(t)$ values and high $^{208}Pb/^{204}Pb$ ratios (Fig. 7), which suggests that the involved components were probably derived from subducted sediments instead of from subducted oceanic crust that commonly has high $\varepsilon_{Nd}(t)$, extremely low Pb and low $^{208}Pb/^{204}Pb$ ratios (Chauvel et al., 2009; Elliott et al., 1997; Hickey-Vargas et al., 2008). In addition, Type-I and -IV mafic dykes are enriched in LREE and Th, denoting that the involved components from subducted sediments are in the form of melts because LREE and Th are immobile in fluids (Hermann et al., 2006). Since LREE and Th are mainly hosted by monazite and/or allanite in subducted sediments, breakdown of these minerals during melting of subducted sediments can result in enrichment of LREE and Th in melts (Fig. 6; Hermann et al., 2006; Todd et al., 2010). Type-I and -IV mafic dykes also have high La/Yb and low Ba/La ratios (Fig. 9), indicating that the melts from subducted sediments are enriched in LREE relative to LILE and HREE. LILE, such as Ba and K, in the subducted sediments are mainly hosted by phengite, while the HREE are buffered by garnet (Hermann and Rubatto, 2009; Spandler and Pirard, 2013; Todd et al., 2010). Depletion of Ba and HREE for type-I and -IV mafic dykes suggest residual phengite and garnet during the melting of subducted sediments, which can also explain the low K_2O content and low K_2O/Na_2O ratio of these mafic dykes. Therefore, Type-I and -IV mafic dykes were derived from the partial melting of the depleted mantle wedge that had been refertilized by the melts from subducted sediments.

Type-II mafic dykes also exhibit significantly positive Pb anomaly (Fig. 6d), consistent with incorporation of the components from subducted sediments. However, they are enriched in Ba and U but depleted in LREE and Th, with high Ba/La and low La/Yb ratios (Fig. 9), which implies that LREE and Th were potentially not mobilized from subducted sediments by the involved agents. In general, LREE and Th are quite mobile in the melt. On the other hand, the fluids from subducted sediments can mobilize LILE at relatively low temperature (<600 °C) (Kessel et al., 2005; Spandler et al., 2007), while monazite and allanite are still stable to retain LREE in subducted sediments (Hermann and Rubatto, 2009; Spandler et al., 2007). Therefore, Type-II mafic dykes would be derived from mantle source metasomatized by fluids from subducted sediments.

5.2.2.2. Melts from subducted oceanic crust. Type-III mafic dykes have high MgO and high $Mg^{\#}$ and show enrichment of Th and LREE with high La/Yb ratios (Fig. 6a), indicating that the input components should be in the form of melts because Th and LREE are mobile elements in melts (Hermann and Rubatto, 2009; Todd et al., 2010). In general, the melts from subducted oceanic crust have depleted Nd—Hf isotopic compositions and cannot significantly change the Nd—Hf isotopic budget of the mantle wedge (Chauvel et al., 2009; Hauff et al., 2003). The high positive $\varepsilon_{Nd}(t)$ and $\varepsilon_{Hf}(t)$ values for Type-III mafic dykes suggest that the input melts in the mantle source were derived from subducted oceanic crust instead of from subducted sediments that generally possess low $\varepsilon_{Nd}(t)$ and $\varepsilon_{Hf}(t)$ values (Chauvel et al., 2009; Hauff et al., 2003; Plank and Langmuir, 1998). This can also account for insignificant Pb anomaly and low $^{208}Pb/^{204}Pb$ ratios of Type-III mafic dykes because of low Pb contents and low $^{208}Pb/^{204}Pb$ ratios in AOC (Chauvel et al., 2009; Elliott et al., 1997; Hickey-Vargas et al., 2008). Since mica is absent during the melting of subducted oceanic crust (Kessel et al., 2005; Klimm et al., 2008), Ba will be released from the oceanic crust (Hermann and Rubatto, 2009), which can explain high Ba/La ratios of Type-III mafic dykes (Fig. 9). Therefore, Type-III mafic dykes were derived from the partial melting of depleted mantle source with input of melts from subducted oceanic crust.

5.2.3. Mechanism for dehydration and melting of subducted slab

The Habahe mafic dykes in a small area (Fig. 2c) show spatial variations in geochemistry due to input of different components from subducted slab into the mantle source, suggesting a sharp change of thermal status of the subducted slab in short distance, which would be due to dehydration and melting of a hot slab subducted beneath the Chinese Altai during the middle Paleozoic (Niu et al., 2006; Yu et al., 2017). The ridge subduction during the middle Paleozoic in the Chinese Altai was proposed to account for the high-temperature metamorphism, large scale felsic magmatism and rapid addition of juvenile materials in the crust of the Chinese Altai (Jiang et al., 2010; Sun et al., 2009; Windley et al., 2007; Xiao et al., 2015). Indeed, melting of subducted slab is a typical process during ridge subduction (DeLong et al., 1978; Johnston and Thorkelson, 1997) because the subducted slab is young and hot as it is located near the oceanic ridge (Defant and Drummond, 1990; DeLong et al., 1978). Furthermore, a slab window may be developed during the ridge subduction because the ridge spreading ceased and unzipped progressively to form a gap (Thorkelson and Breitsprecher, 2005). As close to the slab window, there is a sharp increase of temperature for subducted slab due to ascending of hot sub-slab asthenospheric mantle (Thorkelson and Breitsprecher, 2005). Therefore, the Habahe mafic dykes could be magmatism associated with the middle Paleozoic ridge subduction in the Chinese Altai.

5.3. Chemical fractionation due to dehydration and melting of subducted slab

The Devonian subducted slab in the Chinese Altai underwent multiple stages of dehydration and melting (Yu et al., 2017). The fluids and melts from the subducted slab have distinctive elemental and Sr, Nd, Hf and Pb isotopic compositions (Figs. 6, 7), corresponding to different chemical fractionation processes, which can be deduced by the coupling or decoupling of Sr, Nd, Hf and Pb isotopes in studied samples.

5.3.1. Nd—Hf isotopic decoupling in the subduction zone

Nd—Hf isotopic decoupling was prevailed in metasedimentary rocks, granites and mafic rocks in the Chinese Altai during the middle Paleozoic (Huang et al., 2020; Yu et al., 2017; Zhang et al., 2017), which might be induced by different mechanisms. For example, Nd—Hf isotopic decoupling of S-type granite in the Chinese Altai was likely caused by insufficient dissolution of zircon in disequilibrium melting process (Zhang et al., 2017). But the decoupled Nd—Hf isotopic feature of the middle Paleozoic mafic rocks was attributed to higher mobility of Nd than Hf during the melting of subducted sediments (Yu et al., 2017). The metasedimentary rocks and granites in the Chinese Altai may inherit the Nd—Hf isotopic features of the mantle source because they contain large amount of materials from the mantle-derived magmas (Huang et al., 2020; Yu et al., 2017).

Both Type-I and -IV mafic dykes in this study were derived from the partial melting of mantle source with input of melts from subducted sediments (Fig. 9), and thus show decoupled Nd—Hf isotopes similar

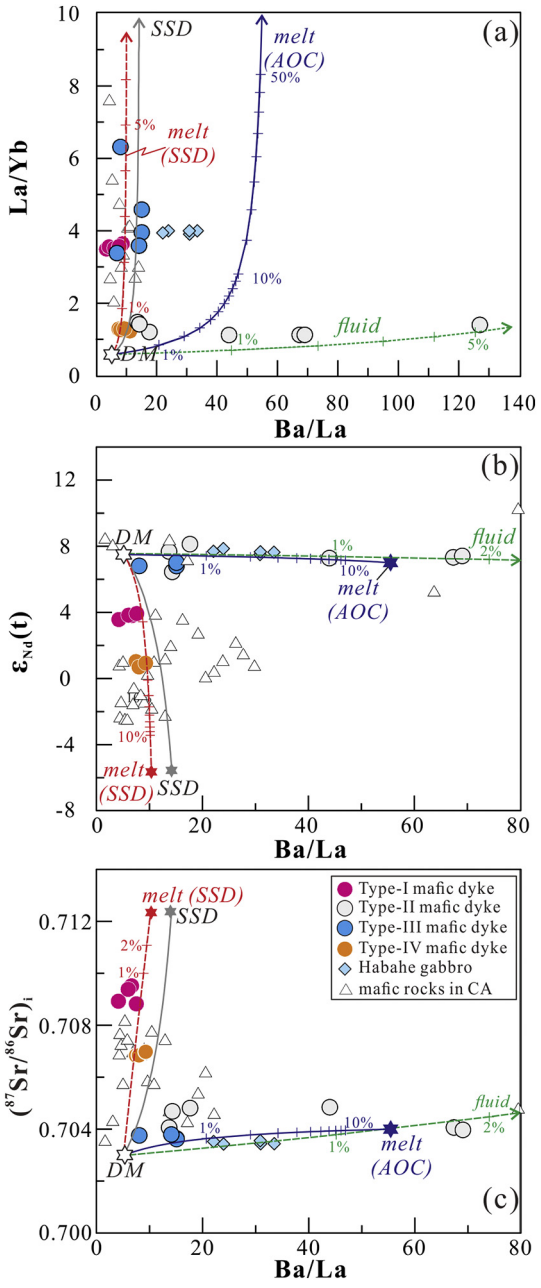

Fig. 9. Diagrams of (a) La/Yb vs. Ba/La, (b) $\varepsilon_{Nd}(t)$ vs. Ba/La and (c) $(^{87}Sr/^{86}Sr)_i$ vs. Ba/La for the Habahe mafic dykes. The Devonian mantle wedge is assumed as the depleted mantle (DM) from Salters and Stracke (2004) (Supplemental Table 5). The Devonian subducted sediments (SSD) in the Chinese Altai are represented by the sedimentary rocks in the Chinese Altai as accretionary complex (Supplemental Table 5). Altered oceanic crust (AOC) is represented by N-MORB from Sun and McDonough (1989). Dehydration and melting conditions of the subducted sediments and basaltic oceanic crust are summarized in Supplemental Table 5.

to the IABs in the hot arcs (Fig. 10a). Since these mafic dykes have low K_2O content (Fig. 8), excluding significant crustal assimilation, their decoupled Nd—Hf isotopic features should not be induced by involvement of crustal materials but inherited from mantle source. In addition, Type-I and -IV mafic dykes all show high positive $\varepsilon_{Hf}(t)$ values, indicating insignificant modification of Hf isotopes in the mantle sources by the components from subducted sediments. In fact, Hf can be retained by zircon that usually behaves as residual mineral during the melting of subducted sediments (Todd et al., 2010). Furthermore, breakdown of monazite can result in high Nd/Hf ratios in the melt, which can introduce more Nd than Hf into the mantle wedge, resulting in the decoupling between Nd and Hf isotopes in the mantle sources for Type-I and -IV mafic dykes (Fig. 10a). In contrast, melts from subducted oceanic crust would inherit the depleted Nd—Hf isotopic compositions, and both Nd and Hf tend to be immobile in fluids. As a result, the melts from subducted oceanic crust and the fluids from subducted sediment cannot significantly alter Nd and Hf isotopes of the mantle wedge (Yu et al., 2017). Therefore, Type-II and -III mafic dykes show coupled and depleted Nd—Hf isotopic feature (Fig. 10a).

5.3.2. Sr—Nd and Sr—Pb isotopic decoupling during melting of subducted sediments

Type-I and -IV mafic dykes show similar Nd, Hf and Pb isotopes but distinctive Sr isotope (Fig. 7). Type-I mafic dykes have higher $(^{87}Sr/^{86}Sr)_i$ ratios than Type-IV mafic dykes and plot on the mixing line between the depleted mantle and the high Sr/Nd and Sr/Pb melts (melt-1 in Fig. 10), indicating that the mantle source for Type-I mafic dykes had been refertilized by the materials with more radiogenic Sr. Due to the high mobility of Sr in melts (Skora and Blundy, 2010), more radiogenic Sr can be transferred from the subducted sediments into the mantle wedge. Sr is commonly buffered by Ca-bearing minerals in subducted sediments, such as plagioclase ($D_{Sr}^{plagioclase} = 4.4$; Bacon and Druitt, 1988), apatite ($D_{Sr}^{apatite} = 2.1$; Watson and Green, 1981) and zoisite ($D_{Sr}^{zoisite} = 2.56$; Feineman et al., 2007). Among them, apatite and zoisite are accessory minerals, while plagioclase is abundant in the modern subducting sediments (Plank and Langmuir, 1998) and would be the most important mineral buffering Sr. The melting of subducted slab commonly occurs under water-saturated conditions due to the breakdown of hydrosilicates (e.g., Zheng et al., 2016). Under water-saturated melting conditions, the plagioclase in subducted sediments might be broken down completely at relatively high pressure (e.g., >7 kbar; Beard and Lofgren, 1991), which results in high Sr content of melts. On the other hand, Nd and Pb will be retained in subducted sediments by monazite (Klimm et al., 2008) and garnet (Stadler et al., 1998) that can survive at relatively high pressure. Therefore, the melts derived from subducted sediments with plagioclase breakdown will have high Sr/Nd and Sr/Pb ratios, indicating a process similar to the formation of adakite (Defant and Drummond, 1990). The incorporation of high Sr/Nd and Sr/Pb melts will modify the mantle wedge more significantly on Sr isotope than on Nd and Pb isotopes, which can result in decoupling between Sr and Nd isotopes and between Sr and Pb isotopes, such as the case of Type-I mafic dykes in this study (Fig. 10).

In contrast, Type-IV mafic dykes have lower $(^{87}Sr/^{86}Sr)_i$ ratios than Type-I mafic dykes, show coupled Sr—Nd or Sr—Pb isotopes and plot on the mixing lines between the depleted mantle and the low Sr/Nd and Sr/Pb melts derived from subducted sediments (Fig. 10). Sr content in the melt is controlled by the Sr concentration of the source and the partition coefficient between the melt and residual phases. Low Sr melts can be generated by partial melting of source with residual plagioclase (Fig. 11b), which is the major mineral hosting Sr in subducted sediments. However, Type-IV mafic dykes emplaced in the north of Type-I mafic dykes, indicating that the subducted sediments were melted at higher pressure due to the northward subduction of the Junggar Ocean underneath the Chinese Altai. If so, plagioclase cannot be a residual phase in subducted sediments because both high water content and high pressure will promote its breakdown (Beard and Lofgren, 1991). Therefore, we suggest that more Sr than Nd and Pb had been transferred from subducted sediments into the overlying mantle wedge during the early stage melting, as shown by high Sr/Nd and Sr/Pb ratios for melts input into the mantle source for Type-I mafic dykes (Fig. 10). After significant extraction of Sr, remelting of the residual low Sr subducted sediments at deeper depth would generate the low Sr melts with low Sr/Nd and Sr/Pb ratios (Fig. 10; Supplemental Table 5), which might carry less radiogenic Sr into the mantle wedge, explaining the low $(^{87}Sr/^{86}Sr)_i$ ratios and insignificant Sr—Nd and Sr—Pb isotopic decoupling for Type-IV mafic dykes in the Chinese Altai (Fig. 10).

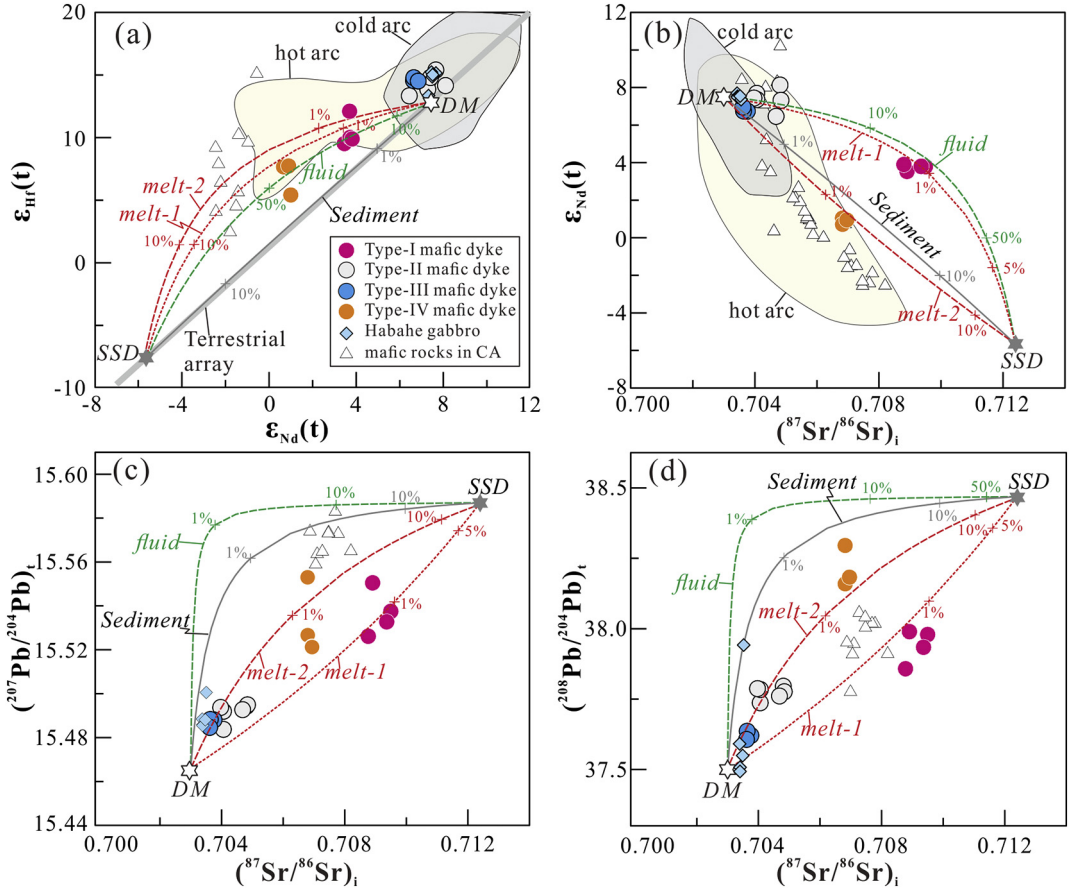

Fig. 10. Diagrams of (a) $\varepsilon_{Hf}(t)$ vs. $\varepsilon_{Nd}(t)$, (b) $\varepsilon_{Nd}(t)$ vs. $(^{87}Sr/^{86}Sr)_i$, (c) $(^{207}Pb/^{204}Pb)_t$ vs. $(^{87}Sr/^{86}Sr)_i$ and (d) $(^{208}Pb/^{204}Pb)_t$ vs. $(^{87}Sr/^{86}Sr)_i$ for the Habahe mafic dykes. Hf isotopic compositions for the Devonian subducted sediments (SSD) and mantle wedge (DM) are calculated based on the terrestrial array ($\varepsilon_{Hf}(t) = \varepsilon_{Nd}(t) \times 1.55 + 1.21$; Vervoort et al., 2011) and assuming $\varepsilon_{Nd}(t) = -5.8$ and $+7.5$, respectively. Pb isotopic compositions for the Devonian mantle wedge and subducted sediments are shown in Supplementary Fig. S3. Melt-1 and melt-2 represent the melts from the subducted sediments in two subduction stages. Dehydration and melting conditions of the subducted sediments are compiled in Supplemental Table 5. "cold arc" includes IAB from the Mariana, Kermadec and New Zealand arcs. "hot arc" is represented by the Sunda, Banda, Lesser Antilles and Luson arcs. Data of IAB are from the PetDB database (http://www.petdb.org).

Type-III mafic dykes show low $(^{87}Sr/^{86}Sr)_i$ ratios, suggesting that the melts from subducted oceanic crust had low $^{87}Sr/^{86}Sr$ ratios (Fig. 10b) and may have not significantly altered the Sr isotopes of mantle wedge. Type-II mafic dykes have higher $(^{87}Sr/^{86}Sr)_i$ ratios than Type-III mafic dykes with similar $\varepsilon_{Nd}(t)$ values (Fig. 10b), suggesting that the fluids from subducted sediments had relatively high Sr/Nd ratios and carried more radiogenic Sr than unradiogenic Nd into their mantle source (Fig. 10b) because Sr is more mobile than Nd in fluids (Hermann et al., 2006; Kessel et al., 2005).

5.4. Missing of Sr—Nd isotopic decoupling in subduction zone

This study shows that with continuous northern subduction of the Junggar Ocean in the middle Paleozoic, fluids and melts were released from the subducted slab and the mantle wedge was modified by such reagents at different subduction depths. At the shallow depth of subduction, melts and fluids from the subducted sediments have high Sr/Nd ratios due to breakdown of plagioclase at shallow subduction depth (Fig. 11), which modified Sr isotope more significantly than Nd isotope of the mantle wedge and caused Sr—Nd isotopic decoupling of Type-I and -II mafic dykes (Fig. 10b). Melts from the subducted sediments were released in two separate stages. Because Sr was mainly extracted by the melts in the early subduction stage, the second stage melts had low Sr/Nd ratios and resulted in coupled Sr—Nd isotopic feature for Type-IV mafic dykes (Fig. 11d). Melts from the subducted oceanic crust have inherited depleted Sr-Nd-Hf-Pb isotopic compositions and led to insignificant Sr-Nd-Hf-Pb isotopic decoupling for Type-III mafic dykes.

Typical IABs are generally characterized by insignificant Sr—Nd isotopic decoupling with plotting below the mixing line between the mantle wedge and melts/fluids derived from subducted sediments (melt-1/fluid-1 in Fig. 12), suggesting negligible chemical fractionation between Sr and Nd during subduction. This phenomenon was once referred as evidence for the physical diapirs of subducted sediments (high-pressure mélange) into the mantle wedge (Nielsen and Marschall, 2017). Type-IV mafic dykes in this study also have insignificant Sr—Nd and Sr—Pb isotopic decoupling (Fig. 10). However, these dykes show significant Nd—Hf isotopic decoupling (Fig. 10a), which indicates that their mantle source had been metasomatized by the melts from subducted sediments. It has been proved that subducted slab will undergo a series of metamorphism or partial melting before sinking to the sub-arc mantle depth (80–160 km) (e.g., Grove and Christy, 2012; Zheng et al., 2016). At a shallow depth (e.g., pressure < 7 kbar), pore-water will be released from subducted slab due to compression. Both Sr and Nd would not be significantly mobilized at this stage due to their very low partition coefficient between fluid and rocks ($D^{fluid/rock}$ values) (4.5E-5 for Sr, and 2.728E-06 for Nd; Mutter et al., 2014). As pressure and temperature increase, the fluids can be further released by the metamorphic dehydration of subducted slab (such as the decomposition of clay minerals or other hydrosilicates) (Fig. 11a). At this stage, plagioclase would be unstable and metamorphosed into jadeite and quartz (Fig. 11a). Since the composition of fluid is controlled by the crystal chemistry of residual

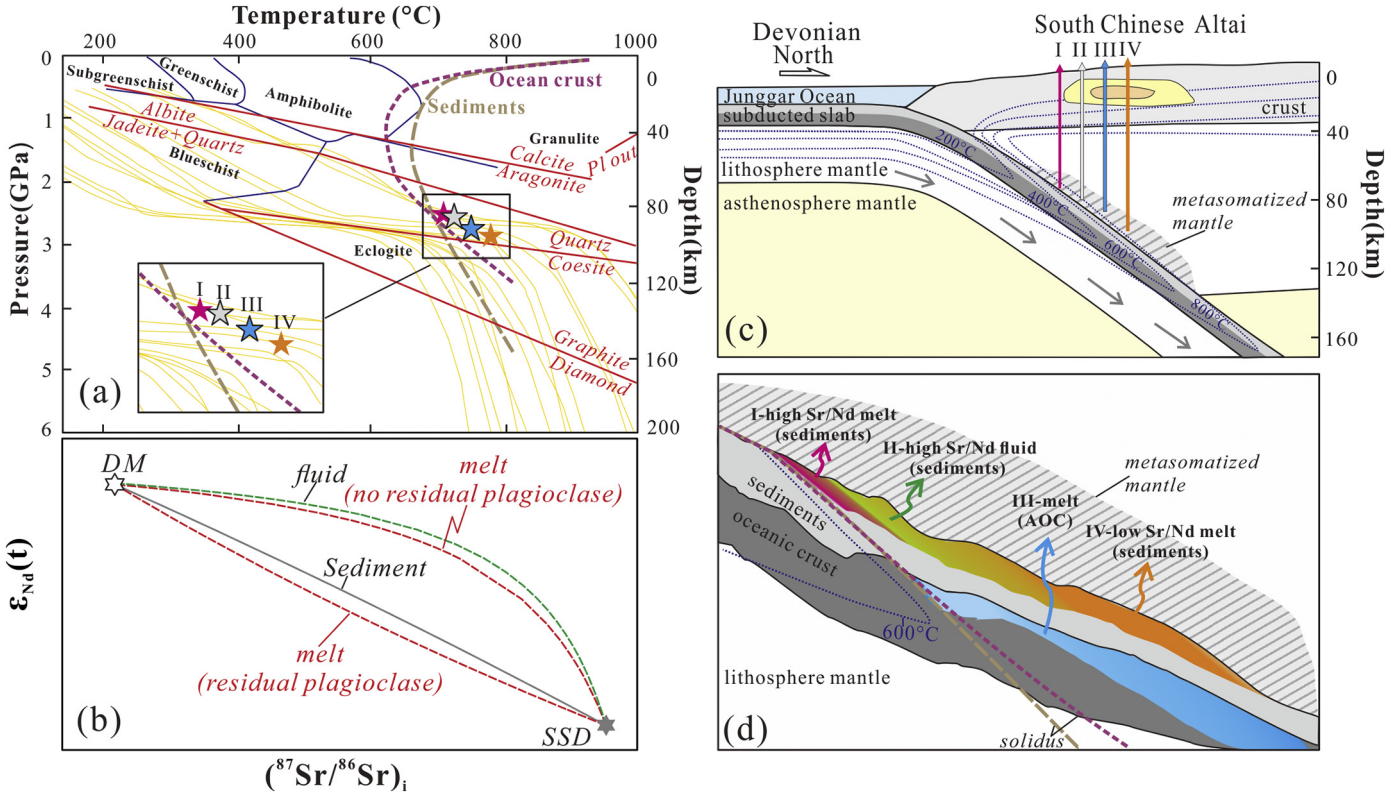

Fig. 11. (a) Pressure-temperature (P-T) diagram for metamorphic faces under subduction-zone conditions, illustrating the range of slab surface P-T conditions (orange lines; Syracuse et al., 2010). The experimentally determined melting curve for H_2O-saturated ocean crust (Liu et al., 1996) (purple curve) and sediment (dark yellow curve; Nichols et al., 1994) were also denoted. (b) Diagram of $\varepsilon_{Nd}(t)$ vs. $(^{87}Sr/^{86}Sr)_i$ shows the mixing trends between the depleted mantle wedge and the fluids and melts from subducted sediments. The detailed melting processes of subducted sediments are compiled in Supplemental Table 5. (c) Cartoon shows petrogenesis of the Habahe mafic dyke due to northward subduction of the Junggar Ocean beneath the south margin of the Chinese Altai in the Devonian. (d) Cartoon characterizes metasomatism of the mantle source for the Habahe mafic dykes with input of different components from subducted slab (AOC and sediments). I, II, III and IV in (c) and (d) represent Type-I, II, III and IV mafic dykes.

phases (Stalder et al., 1998), breakdown of plagioclase can elevate Sr content in fluids (Fig. 11b). The melting of subducted slab at shallow depth can occur in modern hot arcs (Labanieh et al., 2012; Syracuse et al., 2010), which might also result in the complete breakdown of plagioclase due to the high water contents, as shown by Type-I mafic dykes in this study. Therefore, Sr could be fractionated from Nd during the dehydration and melting of a subducted slab at the fore-arc depth, generating high Sr/Nd fluids and melts (Fig. 11b). The input of such fluids and melts will transfer more radiogenic Sr from the subducted sediments into the mantle wedge, resulting in Sr—Nd isotopic decoupling and high $^{87}Sr/^{86}Sr$ ratios in the resultant arc magmas (Fig. 11b; 12).

High-Ca boninites are considered to be derived from the partial melting of lherzolite in the mantle wedge fluxed by fluids from subducted slab at the fore-arc depth (<1 GPa; König et al., 2010). The boninites from the Izu-Bonin-Mariana arc have higher $^{87}Sr/^{86}Sr$ ratios than the typical IABs (Fig. 1), indicating that the fluids from subducted slab at fore-arc depth have higher Sr/Nd ratios. Similarly, the fore-arc basalts have higher $^{87}Sr/^{86}Sr$ ratios than the typical IABs in the Mariana arc and Western Java, which is also consistent with the involvement of high Sr/Nd fluids and melts in the mantle source at the fore-arc depth (Fig. 1). Therefore, chemical fractionation between Sr and Nd in the subduction zone might predominantly occur at the fore-arc. On the other hand, the IABs from representative arcs mostly plot along the mixing line between the mantle wedge and melts/fluids from the low Sr/Nd subducted sediments (melt-2/fluid-2 in Fig. 12). The low Sr/Nd ratios for the subducted sediments at sub-arc depth may be resulted from the loss of more Sr than Nd at the fore-arc, as explicated in this study. The model calculation suggests that if the subducted sediments lose 5% Nd as sinking to sub-arc depth, ca.75%–93% Sr will be required to leave from the subducted sediments to account for the Sr—Nd isotopic compositions of the IABs in most arcs (Fig. 12). These results resemble to the conclusion shown by Type-I and -IV mafic dykes in this study, which suggests that the subducted sediments in the Chinese Altai lost ca. 80% Sr at the first stage melting process (Supplemental Table 5). Consequently, the fluids and melts produced by dehydration and melting of subducted sediments at a sub-arc depth will have much lower Sr/Nd ratios than those at the fore-arc and thus have a smaller effect on fractionating Sr from Nd. The input of such components might not produce significant Sr—Nd isotopic decoupling in the mantle wedge, which explains why the typical IAB from most arcs in the world, as well as Type-IV mafic dykes in this study, do not have significant Sr—Nd isotopic decoupling.

6. Conclusions

The Chinese Altai underwent northward subduction of the Junggar Ocean in the middle Paleozoic and the mantle wedge experienced extensive metasomatism with input of fluids and melts from subducted sediments and melts from oceanic crust. This process is documented by spatial compositional variations of the Habahe mafic dykes that crop out successively from south to north.

Type-I and -IV mafic dykes were all derived from the metasomatized mantle source with input of two different melts from two stages melting of subducted sediments at different subduction depth. Type-I dykes show decoupled Sr—Nd isotopic features due to input of high Sr/Nd melts at the first stage melting of subducted sediments with the breakdown of plagioclase at shallow subduction depth. The coupled Sr—Nd isotopic feature of Type-IV dykes was resulted from input of low Sr/Nd

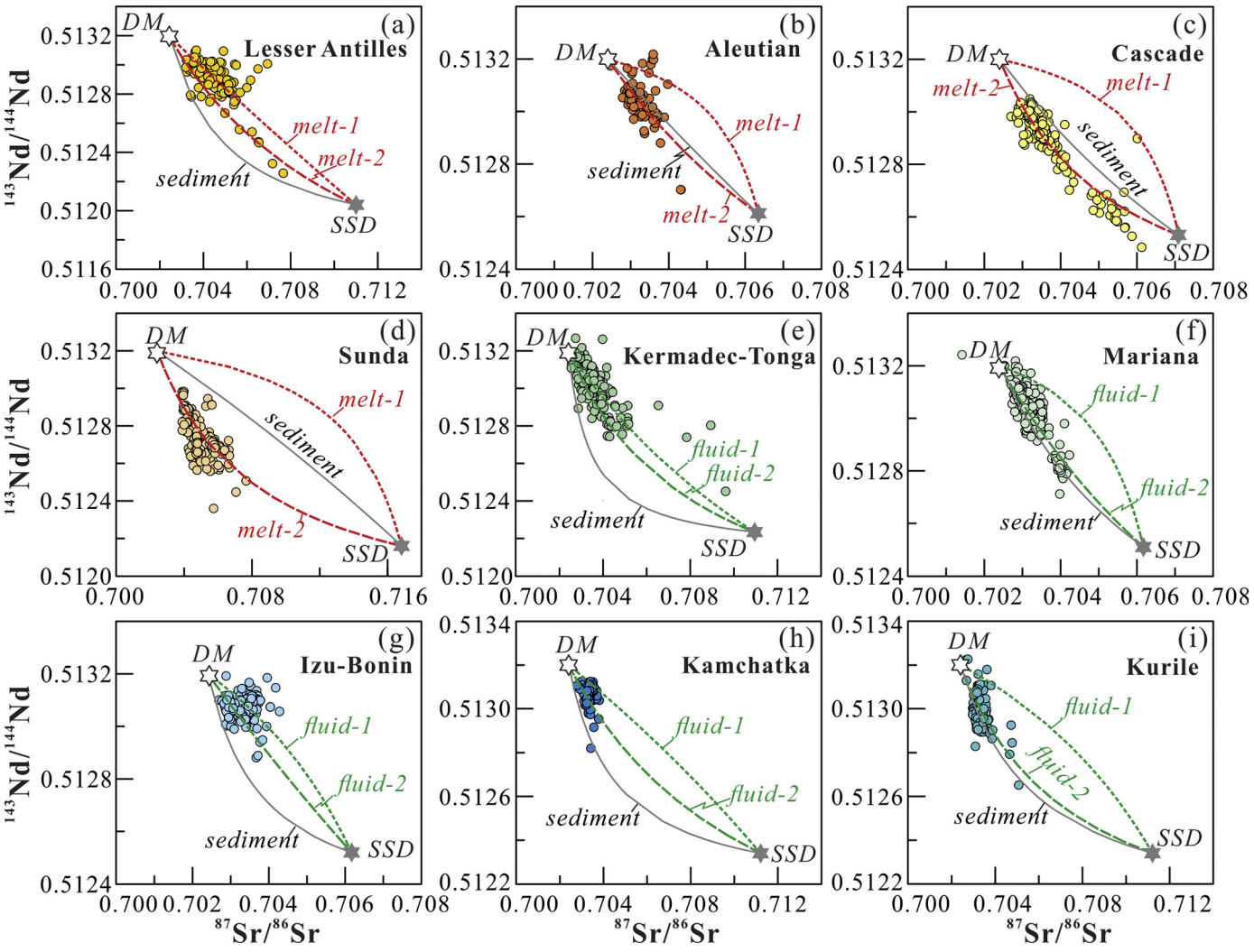

Fig. 12. Diagrams of $\varepsilon_{Nd}(t)$ vs. $(^{87}Sr/^{86}Sr)_i$ for island arc basalts (IAB) of the representative arcs. Melt-1/fluid-1 are generated by melting and dehydration of subducted sediments and melt-2/fluid-2 represent the melts/fluids from subducted sediments with significant loss of Sr at sub-arc depth. The mantle wedge is represented by the depleted mantle (DM) from Salters and Stracke (2004). The data of IAB and subducted sediments (SSD) of the representative arcs are from the PetDB database (http://www.petdb.org) and Plank and Langmuir (1998), respectively. Dehydration and melting conditions of the subducted sediments for these arcs are as Fig. 8.

melts from the second stage melting of subducted sediments which underwent significant loss of Sr in the early subduction stage. This mechanism can also explain higher $^{86}Sr/^{87}Sr$ for fore-arc basalt and boninite than IAB, indicating that fractionation between Sr and Nd dominantly occurs at the fore-arc.

Type-III mafic dykes were originated from the depleted mantle source metasomatized by melts from subducted oceanic crust. The depleted Sr-Nd-Hf-Pb isotopic compositions of these samples suggest insignificant modification of their mantle source in these isotope systems.

Supplementary data to this article can be found online at https://doi.org/10.1016/j.lithos.2020.105465.

Declaration of Competing Interest

The authors declare that they have no known competing financial interests or personal relationships that could have appeared to influence the work reported in this paper.

Acknowledgments

We thank L. Zhang, S.L. Sun, Q. Yang, X.P. Xia and X.L. Tu for analytical assistance. We gratefully acknowledge the constructive comments of Prof. T. Wang and an anonymous reviewer, which considerably improved this contribution, and appreciate Prof. X.H. Li for editorial handling. This study was financially supported by the National Natural Science Foundation of China (NSFC Projects 41625007, 41902056), Hong Kong RGC grants (17303415, 17302317), and China Postdoctoral Science Foundation (2018M633172). This is a contribution of the Joint Laboratory of Chemical Geodynamics between HKU and CAS (Guangzhou Institute of Geochemistry) to IGCP 592. This is contribution No. IS-2827 from GIG-CAS.

References

Bacon, C.R., Druitt, T.H., 1988. Compositional Evolution of the Zoned Calcalkaline Magma Chamber of Mount-Mazama, Crater Lake, Oregon. Contrib. Mineral. Petrol. 98 (2), 224–256.

Beard, J.S., Lofgren, G.E., 1991. Dehydration melting and water-saturated melting of basaltic and andesitic greenstones and amphibolites at 1, 3, and 6.9 kbar. J. Petrol. 32, 365–401.

Cai, K.D., Sun, M., Yuan, C., Zhao, G.C., Xiao, W.J., Long, X.P., Wu, F.Y., 2010. Geochronological and geochemical study of mafic dykes from the northwest Chinese Altai: Implications for petrogenesis and tectonic evolution. Gondw. Res. 18, 638–652.

Chauvel, C., Marini, J.C., Plank, T., Ludden, J.N., 2009. Hf-Nd input flux in the Izu-Mariana subduction zone and recycling of subducted material in the mantle. Geochem. Geophys. Geosyst. 10 (1). https://doi.org/10.1029/2008GC002101.

Defant, M.J., Drummond, M.S., 1990. Derivation of some modern arc magmas by melting of young subducted lithosphere. Nature 347, 662–665.
DeLong, S.E., Fox, P.J., McDowell, F.W., 1978. Subduction of the Kula ridge at the Aleutian trench. Geol. Soc. Am. Bull. 89, 83–95.
Dunn, T., Sen, C., 1994. Mineral/matrix partition-coefficients for orthopyroxene, plagioclase, and olivine in basaltic to andesitic systems - a combined analytical and experimental-study. Geochim. Cosmochim. Acta 58 (2), 717–733. https://doi.org/10.1016/0016-7037(94)90501-0.
Elliott, T., Plank, T., Zindler, A., White, W., Bourdon, B., 1997. Element transport from slab to volcanic front at the Mariana Arc. J. Geophys. Res. 102 (7), 14991–15019.
Feineman, M., Ryerson, F., Depaulo, D., Plank, T., 2007. Zoisite-aqueous fluid trace element partitioning with implications for subduction zone fluid composition. Chem. Geol. 239, 250–265.
Foley, S.F., Barth, M.G., Jenner, G.A., 2000. Rutile/melt partition coefficients for trace elements and an assessment of the influence of rutile on the trace element characteristics of subduction zone magmas. Geochim. Cosmochim. Acta 64 (5), 933–938.
Green, T., Blundy, J., Adam, J., Yaxley, G., 2000. SIMS determination of trace element partition coefficients between garnet, clinopyroxene and hydrous basaltic liquids at 2–7.5 Gpa and 1080–1200°C. Lithos 53, 165–187.
Grove, T.L., Christy, B.T., 2012. The role of H_2O in subduction zone magmatism. Annu. Rev. Earth Planet. Sci. 40, 413–439.
Hauff, F., Hoernle, K., Schmidt, A., 2003. Sr-Nd-Pb composition of Mesozoic Pacific oceanic crust (Site 1149 and 801, ODP Leg 185), Implications for alteration of ocean crust and the input into the Izu-Bonin-Mariana subduction system. Geochem. Geophys. Geosyst. 4 (8), 8913. https://doi.org/10.1029/2002GC000421.
Hermann, J., Rubatto, D., 2009. Accessory phase control on the trace element signature of sediment melts in subduction zones. Chem. Geol. 265, 512–526.
Hermann, J., Spandler, C., Hack, A., Korsakov, A.V., 2006. Aqueous fluids and hydrous melts in high-pressure and ultra-high pressure rocks: Implications for element transfer in subduction zones. Lithos 92, 399–417.
Hickey-Vargas, R., Bizimis, M., Deschamps, A., 2008. Onset of the Indian Ocean isotopic signature in the Philippine Sea Plate: Hf and Pb isotope evidence from early cretaceous terranes. Earth Planet. Sci. Lett. 268, 255–267.
Hoernle, K., 1998. Geochemistry of Jurassic oceanic crust beneath Gran Canaria (Canary Islands): Implications for crustal recycling and assimilation. J. Petrol. 39, 859–880.
Huang, Y.Q., Jiang, Y.D., Yu, Y., Collett, S., Wang, S., Shu, T., Xu, K., 2020. Nd-Hf isotopic decoupling of the Silurian-Devonian granitoids in the Chinese Altai: a consequence of crustal recycling of the Ordovician accretionary wedge? J. Earth Sci. 31, 102–114.
Jahn, B.M., Wu, F.Y., Chen, B., 2000. Granitoids of the Central Asian Orogenic Belt and continental growth in the Phanerozoic. Trans. R. Soc. Edinb. Earth Sci. 91, 181–193.
Jiang, Y.D., Sun, M., Zhao, G.C., Yuan, C., Xiao, W.J., Xiao, X.P., Long, X.P., Wu, F.Y., 2010. The 390 Ma high-T metamorphism in the Chinese Altai: consequence of ridge subduction? Am. J. Sci. 310, 1421–1452.
Johnson, K.T.M., 1998. Experimental determination of partition coefficients for rare earth and high-field-strength elements between clinopyroxene, garnet, and basaltic melt at high pressure. Contrib. Mineral. Petrol. 133 (1–2), 60–68.
Johnston, S.T., Thorkelson, D.J., 1997. Cocos-Nazca slab window beneath Central America. Earth Planet. Sci. Lett. 146, 465–474.
Kelley, K.A., Plank, T., Ludden, J., Staudigel, H., 2003. Composition of altered oceanic crust at ODP sites 801 and 1149. Geochem. Geophys. Geosyst. 4 (6), 8910. https://doi.org/10.1029/2002GC000435.
Kessel, R., Schmidt, M.W., Ulmer, P., Pettke, T., 2005. Trace element signature of subduction-zone fluids, melts and supercritical liquids at 120–180 km depth. Nature 437, 724–727.
Klimm, K., Blundy, J.D., Green, T.H., 2008. Trace element partitioning and accessory phase saturation during H_2O-saturated melting of basalt with implications for subduction zone chemical fluxes. J. Petrol. 49, 523–553.
König, S., Münker, C., Schuth, S., Luguet, A., Hoffmann, J.E., Kuduon, J., 2010. Boninites as windows into trace element mobility in subduction zones. Geochim. Cosmochim. Acta 74 (2), 684–704.
Kröner, A., Kovach, V., Alexeiev, D., Wang, K., Wong, J., Degtyarev, K., Kozakov, I., 2017. No excessive crustal growth in the Central Asian Orogenic Belt: further evidence from field relationships and isotopic data. Gondw. Res. 50, 135–166.
Labanieh, S., Chauvel, C., Germa, A., Quidelleur, X., 2012. Martinique: a clear case for sediment melting and slab dehydration as a function of distance to the trench. J. Petrol. 53 (12), 2441–2464.
Li, X., Tang, G., Gong, B., Yang, Y., Hou, K., Hu, Z., Li, Q., Liu, Y., Li, W., 2013. Qinghu zircon: a working reference for microbeam analysis of U-Pb age and Hf and O isotopes. Chin. Sci. Bull. 58, 4647–4654.
Li, P.F., Sun, M., Shu, C.T., Yuan, C., Jiang, Y.D., Zhang, L., Cai, K.D., 2019. Evolution of the Central Asian Orogenic Belt along the Siberian margin from Neoproterozoic-early Paleozoic accretion to Devonian trench retreat and a comparison with Phanerozoic eastern Australia. Earth Sci. Rev. 198, 102951.
Liu, J., Bohlen, S.R., Ernst, W.G., 1996. Stability of hydrous phases in subducting oceanic crust. Earth Planet. Sci. Lett. 143, 161–171.
Ludwig, K.R., 2008. Isoplot 3.6. Berkeley Geochronology Center Special Publication No.4 p. 77.
McDonough, W.F., Sun, S.S., 1995. The composition of the Earth. Chem. Geol. 120, 223–253.
Mutter, A., Holzheid, A., Klügel, A., Wilke, M., Berndt, J., Garbe-Schönberg, D., 2014. Element signatures of subduction-zone fluids. An experimental study of the element partitioning ($D^{fluid/rock}$) of natural partly altered igneous rocks from the ODP drilling site 1256. Int. J. Earth Sci. 103, 1917–1927.
Nichols, G.T., Wyllie, P.J., Stern, C.R., 1994. Subduction zone melting of pelagic sediments constrained by melting experiments. Nature 371, 785–788.
Nielsen, S.G., Marschall, H.R., 2017. Geochemical evidence for mélange melting in global arcs. Sci. Adv. 3 (4). https://doi.org/10.1126/sciadv.1602402.
Niu, H.C., Hiroaki, S., Zhang, H.X., Ito, J., Yu, X.Y., Nagao, T., Terada, K., Zhang, Q., 2006. Juxtaposition of adakite, boninite, high-TiO_2 and low-TiO_2 basalts in the Devonian southern Altay, Xinjiang, NW China. J. Asian Earth Sci. 28, 439–456.
Plank, T., Langmuir, C.H., 1998. The chemical composition of subducting sediment: implications for the crust and mantle. Chem. Geol. 145, 325–394.
Vervoort, J.D., Plank, T., Prytulak, J., 2011. The Hf-Nd isotopic composition of marine sediments. Geochim. Cosmochim. Acta 75, 5903–5926.
Reagan, M.K., Ishizuka, O., Stern, R.J., Kelley, K.A., Lacasse, C., Blichert-Toft, J., Bloomer, S.H., Cash, J., Fryer, P.B., Hanan, B.B., Hickey-Vargas, R., Ishii, T., Kimura, J.I., Peate, D.W., Rowe, M.C., Woods, M., 2010. Fore-arc basalts and subduction initiation in the Izu-Bonin-Mariana systems? Geochem. Geophys. Geosyst. 11. https://doi.org/10.1029/2009GC002871.
Salters, V.J.M., Stracke, A., 2004. Composition of the depleted mantle. Geochem. Geophys. Geosyst. 5 (5). https://doi.org/10.1029/2003GC000597.
Sendjaja, Y.A., Kimura, J.I., Sunardi, E., 2009. Across-arc geochemical variation of Quaternary lavas in West Java, Indonesia: mass-balance elucidation using arc basalt simulator model. Island Arc 18, 201–224.
Skora, S., Blundy, J., 2010. High-pressure hydrous phase relations of radiolarian clay and implications for the involvement of subducted sediment in arc magmatism. J. Petrol. 51, 2211–2243.
Spandler, C., Pirard, C., 2013. Element recycling from subducting slabs to arc crust: a review. Lithos 170, 208–223.
Spandler, C., Mavrogenes, J., Hermann, J., 2007. Experimental constraints on element mobility from subducted sediments using high-P synthetic fluid/melt inclusions. Chem. Geol. 239, 228–249.
Stalder, R., Foley, S.F., Brey, G.P., Horn, I., 1998. Mineral aqueous fluid partitioning of trace elements at 900-1200 degrees C and 3.0–5.7 GPa: New experimental data for garnet, clinopyroxene, and rutile, and implications for mantle metasomatism. Geochim. Cosmochim. Acta 62 (10), 1781–1801.
Sun, S.S., McDonough, W.F., 1989. Chemical and isotopic systematics of oceanic basalts: implication for mantle composition and process. In: Sauders, A.D., Norry, M.J. (Eds.), Magmatism in the Ocean Basins. Specical Publications 42. Geological Society, London, pp. 313–345.
Sun, M., Yuan, C., Xiao, W., Long, X., Xia, X., Zhao, G., Lin, S., Wu, F., Kröner, A., 2008. Zircon U-Pb and Hf isotopic study of gneissic rocks from the Chinese Altai: progressive accretionary history in the early to middle Palaeozoic. Chem. Geol. 247, 352–383.
Sun, M., Long, X.P., Cai, K.D., Jiang, Y.D., Wang, B., Yuan, C., Zhao, G.C., Xiao, W.J., Wu, F.Y., 2009. Early Paleozoic ridge subduction in the Chinese Altai: Insight from the abrupt change in zircon Hf isotopic compositions. Sci. China Ser. D 52, 1345–1358.
Syracuse, E.M., van Keken, P.E., Abers, G.A., 2010. The global range of subduction zone thermal models. Phys. Earth Planet. In. 183, 73–90.
Thorkelson, D.J., Breitsprecher, K., 2005. Partial melting of slab window margins: genesis of adakitic and non-adakitic magmas. Lithos 79, 25–41.
Todd, E., Gill, J.B., Wysoczanski, R.J., Handler, M.R., Wright, I.C., Gamble, J.A., 2010. Sources of constructional cross-chain volcanism in the southern Havre Trough: New insights from HFSE and REE concentration and isotope systematics. Geochem. Geophys. Geosyst. 11 (4). https://doi.org/10.1029/2009GC002888.
Wang, T., Jahn, B.M., Kovach, V.P., Tong, Y., Hong, D.W., Han, B.F., 2009. Nd-Sr isotopic mapping of the Chinese Altai and implications for continental growth in the Central Asian Orogenic Belt. Lithos 110, 359–372.
Watson, E.B., Green, T.H., 1981. Apatite/liquid partition coefficients for the rare earth elements and strontium. Earth Planet. Sci. Lett. 56, 405–421.
Windley, B.F., Kroner, A., Guo, J.H., Qu, G.S., Li, Y.Y., Zhang, C., 2002. Neoproterozoic to Paleozoic geology of the Altai orogen, NW China: new zircon age data and tectonic evolution. J. Geol. 110, 719–737.
Windley, B.F., Alexeiev, D., Xiao, W.J., Kroner, A., Badarch, G., 2007. Tectonic models for accretion of the Central Asian Orogenic Belt. J. Geol. Soc. London 164, 31–47.
Woodhead, J.D., Hergt, J.M., Davidson, J.P., Eggins, S.M., 2001. Hafnium isotope evidence for 'conservative' element mobility during subduction zone processes. Earth Planet. Sci. Lett. 192, 331–346.
Xiao, W.J., Windley, B.F., Badarch, G., Sun, S., Li, J., Qin, K., Wang, Z., 2004. Palaeozoic accretionary and convergent tectonics of the southern Altaids: implications for the growth of Central Asia. J. Geol. Soc. Lond. 161, 339–342.
Xiao, W.J., Windley, B., Sun, S., Li, J.L., Huang, B.C., Han, C.M., Yuan, C., Sun, M., Chen, H.L., 2015. A tale of amalgamation of three Permo-Triassic collage systems in Central Asia: oroclines, sutures, and terminal accretion. Annu. Rev. Earth Planet. Sci. 43, 407–507.
Yu, Y., Sun, M., Huang, X.L., Zhao, G.C., Li, P.F., Long, X.P., Cai, K.D., Xia, X.P., 2017. Sr-Nd-Hf-Pb isotopic evidence for modification of the Devonian lithospheric mantle beneath the Chinese Altai. Lithos 284–285, 207–221.
Yu, Y., Sun, M., Yuan, C., Zhao, G.C., Huang, X.L., Rojas-Agramonte, Y., Chen, Q., 2019. Evolution of the middle Paleozoic magmatism in the Chinese Altai: constraints on the crustal differentiation at shallow depth in the accretionary orogen. J. Asian Earth Sci. 175, 230–246.
Zhang, J.J., Wang, Q., Tong, Y., Zhang, Z.C., Song, P., Zhang, L., Huang, H., Guo, L., Hou, Z.Q., 2017. Tracking deep ancient crustal components by xenocrystic/inherited zircons of Palaeozoic felsic igneous rocks from the Altai-East Junggar terrane and adjacent regions, western Central Asian Orogenic Belt and its tectonic significance. Int. Geol. Rev. 59 (16), 2021–2040.
Zheng, Y.F., Chen, R.X., Xu, Z., Zhang, S.B., 2016. The transport of water in subduction zones. Sci. China Earth Sci. 59, 651–682.